J Mater Sci (2023) 58:13398–13421

Metals & corrosion

Using defects as a 'fossil record' to help interpret complex processes during additive manufacturing: as applied to raster-scanned electron beam powder bed additively manufactured Ti–6Al–4V

Katie O'Donnell[1], Maria J. Quintana[1,2], Matthew J. Kenney[1], and Peter C. Collins[1,2,*]

[1] *Department of Materials Science and Engineering, Iowa State University, 528 Bissell Rd, Ames, IA 50011, USA*
[2] *Ames Laboratory, Ames, IA 50011, USA*

Received: 25 April 2023
Accepted: 5 August 2023
Published online: 27 August 2023

ABSTRACT

Defects in parts produced by additive manufacturing, instead of simply being perceived as deleterious, can act as important sources of information associated with the complex physical processes that occur during materials deposition and subsequent thermal cycles. Indeed, they act as materials-state 'fossil' records of the dynamic AM process. The approach of using defects as epoch-like records of prior history has been developed while studying additively manufactured Ti–6Al–4V and has given new insights into processes that may otherwise remain either obscured or unquantified. Analogous to 'epochs,' the evolution of these defects often is characterized by physics that span across a temporal length scale. To demonstrate this approach, a broad range of analyses including optical and electron microscopy, X-ray computed tomography, energy-dispersive spectroscopy, and electron backscatter diffraction have been used to characterize a raster-scanned electron beam Ti–6Al–4V sample. These analysis techniques provide key characteristics of defects such as their morphology, location within the part, complex compositional fields interacting with the defects, and structures on the free surfaces of defects. Observed defects have been classified as banding, spherical porosity, and lack of fusion. Banding is directly related to preferential evaporation of Al, which has an influence on mechanical properties. Lack-of-fusion defects can be used to understand columnar grain growth, fluid flow of melt pools, humping, and spattering events.

Handling Editor: P. Nash.

Katie O'Donnell and Maria J. Quintana have contributed equally.

Address correspondence to E-mail: pcollins@iastate.edu

E-mail Addresses: katieo1@iastate.edu; mariaqh@iastate.edu

https://doi.org/10.1007/s10853-023-08838-0

GRAPHICAL ABSTRACT

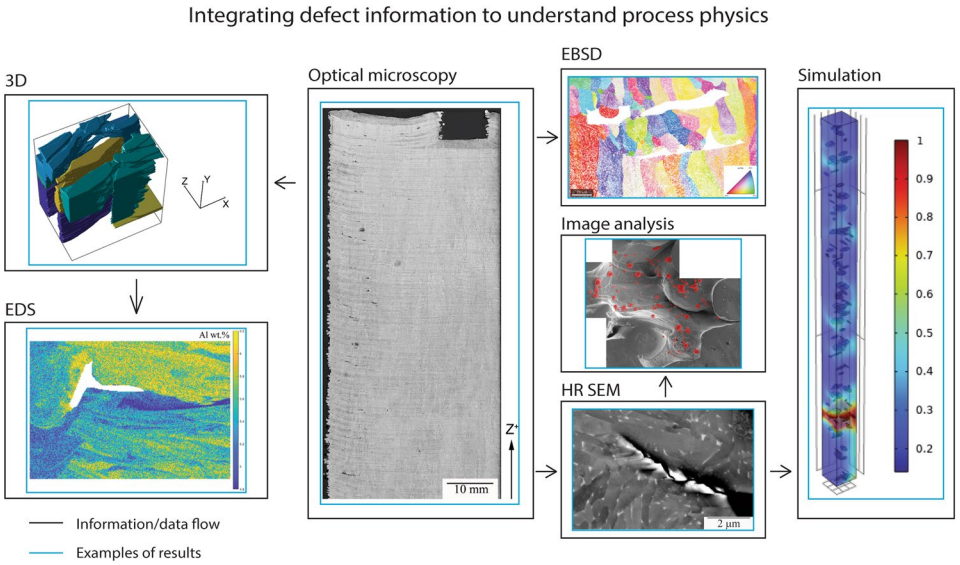

Introduction

Metals-based additive manufacturing (AM) has evolved considerably since the early systems due to both technological advancements (hardware) and improved computer-aided design tools (software). For the last 20 years, researchers have sought to understand the complex physics associated with the prototypical layer-by-layer nature of AM processes and the influence of various AM methods, process parameters, and melting strategies on final parts [1–13]. However, while great insights have been made in recent years (e.g., [14–19]), many details remain hidden from sight, lying beneath the surface of the molten pool. Efforts to probe details such as melt pool dynamics and defect formation are hindered due to experimental limitations, including spatial and temporal resolutions, the opacity of the molten pool, complex temperature fields, and the fact that the material is intrinsically non-uniform in respect to temperature, density, composition with anisotropic, spatially varying thermophysical properties of all types.

Briefly, additive manufacturing has many benefits over traditional manufacturing processes, including a reduction in manufacturing time, the enablement of complex and customized geometries, and the potential to create multi-material parts [20, 21] or materials with hybrid and/or meta-material characteristics [22, 23]. Within the wider titanium community, it is accepted that AM significantly reduces the buy-to-fly ratio, eliminating the conversion of high-valued starting material into waste [20].

For the case of metals and alloys, various fusion-based AM techniques are available and can be categorized according to, among other characteristics, their feed-stock and material delivery systems (e.g., wire-fed, powder-blown, or powder bed processes), and energy sources or variants (e.g., laser beam, electron beam, laser hot wire) [2, 20]. When considering physical phenomena, similarities exist between those active during these manufacturing methods and those active during casting, welding, or other thermomechanical processes. However, AM is sufficiently different so that any assumptions of local thermal equilibrium must be rejected, and the various equations, models, and simulation tools developed for these traditional metals processing routes cannot be applied directly [2, 24–27], or, if applied, have non-trivial uncertainties associated with the predicted outputs. To overcome these basic science/knowledge gaps, efforts are underway to better understand the physical processes that occur dynamically during the thermal cycling within an AM process, including finite element modeling of the thermal conditions [28, 29], in situ observations of the build processes [30, 31], and post-build analyses of resulting characteristics such as texture, microstructure, and materials properties [2, 24]. By comparing certain characteristics of the materials state [13, 32–34],

including those typically considered to be detrimental (e.g., pores, lack-of-fusion defects), studying features that give insights into the physical and thermomechanical mechanisms at play [11] during AM processes is possible.

The nature of AM powder bed fusion processes is such that local regions experience multiple temperature cycles as a result of the layer-by-layer approach, which can result in materials whose mechanical properties are not only anisotropic, but also spatially heterogeneous [35–42]. These variations are due to several factors, including, but not limited to: (i) the remelting and/or reheating of volumes due to continued deposition; (ii) the scan strategies themselves, which can be varied and include both raster scan and spot scan; and (iii) the materials thermophysical properties. These factors will have an influence on heat and mass transport, fluid flow, geometry and size of melt pool, and vapor plume, among others.

Microstructural defects in AM are generally attributed to a combination of one or more unintentional variations of composition, process (e.g., powder layer thickness, heat input), or external materials interacting with the melt pool during the process (e.g., gasses in the build chamber or from within the powder particles, powder/wire contamination) [1, 2, 43]. High thermal gradients can lead to non-uniform vaporization of elements (including contaminants) from the raw materials [2, 11, 30]. Fluid dynamics of melt pools can lead to solute segregation and movement of pores (keyholing, dragging bubbles to the tail end of melt pools, etc.) [2, 11, 21]. Compositional variations can lead to microstructural characteristics [2, 11, 20], such as banding, which results in anisotropic properties across layers, while effects from fluid dynamics can lead to anisotropy within a single layer.

Some of the most commonly studied defects in powder-based AM processes are voids and pores (i.e., lack-of-fusion defects, keyhole pores, gas porosity), and cracks of various types (i.e., hot tearing, liquation cracking, or cracking arising from thermomechanical cycling). Lack-of-fusion (LOF) defects in AM are a result of incomplete fusion of the material by the heat source by either insufficient melt pool overlap within layers, improper wetting, or insufficient melt pool penetration [44]. Keyhole pores are created when heat sources with a sufficiently high power vaporize a portion of the sample, leaving behind bubbles of different sizes that are typically spherical in nature for raster scan strategies [2]. Gas porosity is also spherical in nature, but results from entrapped gases, from the build chamber (in laser based processes, since electron beam processes are performed in vacuum), the powder itself, or volatilization and condensation of lower boing point metallic species [45–48].

In general, LOF defects negatively impact mechanical properties, and in extreme cases (i.e., large defects, sharp corners of the defect(s), unmelted powder particles, contaminants) can lead to high stress concentrations and eventually unexpected or early failure of the part [1, 20]. Thermal cycles, including those happening during AM, are known to generate stresses, and if the thermal properties of the material cannot accommodate these stresses, or the geometry includes sharp corners (either the geometry of the part or the geometries of defects generated during the build process), cracks can be formed, which can limit the use of the part [49, 50]. Separately, hot cracking can occur for a number of reasons, including: in alloys with mechanical and/or thermal constraints (i.e., high solidification shrinkage or large thermal contraction), when liquid is trapped between dendrites or liquid films are present along grain/nuclei boundaries (liquation cracking), or by excessive energy input [19, 51–53]. There is a dearth of literature on additive manufacturing that links LOF defects and the complex and interconnected physical mechanisms that are associated with the AM process (e.g., liquid flow, Marangoni convection, wetting), their formation, and their evolution.

This work presents observations from different types of defects and interprets their salient characteristics to reveal information about the physical mechanisms that are operating in a rastered electron beam melted (EBM) powder bed AM Ti–6Al–4V part. For example, compositional analysis of microstructural variations, and the way these variations interact with defects within a layer, can reveal information about fluid flow in AM builds, including solute variations within the liquid state. Conversely, relationships between microstructural defects such as banding can be an indicator of vaporization of select elements, in this case aluminum, which influence the mechanical properties of the material. Non-destructive evaluation using X-ray Computed Tomography can give insights into shape, sizes, and the distribution of defects and potentially determine regions of interest for further analyses and highlight differences in process phenomena which can lead to their non-random distributions. Lack-of-fusion defects have a large influence on columnar grain growth in the β temperature region

for Ti–6Al–4V. The presence of lack-of-fusion defects is related to spatial–temporal variations in energy (for a given volume), which is commonly related to the electron beam slowing down when changing direction, as well as to the interactions of new melt pools with already contoured regions, as these defects are primarily located at the sample edges. However, there may be other causes. The LOF defects represent submerged (or partially submerged) defects, and thus can provide exceptional 'fossil' records of phenomena such as surface rippling (i.e., humping) or spattering, as well as acting as markers of local thermal conditions and thermal cyclic history. These observations record events that occurred at those locations that would be difficult to analyze using conventional or even emerging in situ monitoring sensors. Thus, we can draw new insights into not only the defects themselves, but associated features that can permit either the further optimization of process conditions or the improvement of multiphysics models of the process itself.

Experimental procedure

Ti–6Al–4V square prisms (15 mm (X) x 15 mm (Y) x 25 mm (Z, build direction)) were produced at Oak Ridge National Laboratory Manufacturing Demonstration Facility (ORNL MDF) using an ARCAM EBM Q10plus system. The build chamber was kept at a pressure of 4.5×10^{-2}mBar and a preheat temperature of 470 °C. A stainless steel build plate and TEKNA plasma atomized powder with a particle size ranging from 45 to 105 μm (−140/ + 325 mesh) used during the build. The layer thickness was 50 μm. The scan strategy that was adopted for these samples was a linear raster (serpentine) scan at a speed of 4550 mm s^{-1}. The incident beam was set so that it had a beam current of 28 mA and a beam power of 1200W. Before the electron beam started rastering across a layer, a contouring scanning strategy melted the edges of each layer. The raster path direction was rotated by 67.5° after each layer.

The as-built samples were sectioned vertically using electrical discharge machining (EDM). The EDM'd surfaces were ground and polished using traditional metallographic sample preparation techniques, completely removing the EDM recast layer. Samples were imaged using an FEI Teneo LoVac field-emission scanning electron microscope (SEM) equipped with both energy-dispersive spectroscopy (EDS) and electron backscatter diffraction (EBSD) from Oxford analytical instruments. Optical microscopy (OM) mosaics were obtained using a Zeiss inverted optical metallographic microscope after the sample was etched with Kroll's reagent. SEM images and EDS and EBSD maps were acquired with the same settings, 20 kV and 0.8nA. EDS maps were collected using a grid of 256 × 176 pixels; EBSD maps had a step size of 0.5 μm. SEM images were used to characterize microstructural features such as basketweave volume fraction and α lath width, as described in [54–56].

Two 1.5 mm × 1.5 mm × 12.5 mm 'toothpick'-like sub-scale volumes were excised from one of the edges of one sample using commercial precision EDM machining and analyzed with a 225 kV X-ray computed tomography (CT) system, with a reconstruction voxel size of 6 μm × 6 μm ×12 μm. Afterward, these small volumes were serially sectioned, polished, etched using Kroll's reagent, and imaged using a Robo-Met.3D® system [57] equipped with a Zeiss optical microscope and capable of optical serial sectioning by repeated and computer-controlled grinding, polishing, etching, and imaging to provide data for subsequent three-dimensional reconstruction. Images from all three analysis methods (OM, SEM, and CT) were analyzed using MIPAR image analysis software [58], including the 3D reconstruction using the integrated 3D Toolbox. MATLAB was used to plot EDS maps for easier comparison, and the MTEX 5.7.0 toolbox [59] within MATLAB was used for analysis of EBSD results.

Additionally, powder used for the manufacture of these builds was analyzed using the FEI SEM in both its virgin (unused) and used (from the build chamber) states. To investigate the effect of thermal history on free surfaces of Ti–6Al–4V particles, unused powder was wrapped in pure titanium foil, sealed in glass ampules under argon and with a piece of pure titanium sponge (to prevent/minimize oxidation), and sintered for two hours. One ampule was sintered at 925 °C, below the β-transus temperature, while a second ampule was sintered at 1025 °C, above the β-transus. The resulting sintered powders were also imaged in the SEM.

COMSOL Multiphysics® software, version 6.0 (released December 2021), was used to conduct finite element simulations, invoking the structural mechanics physics and linear elastic module nodes to simulate various physics within the Ti–6Al–4V sample. Specifically, the damage subnode was used to analyze

results under tensile forces, modeled as a prescribed displacement. The sides of the modeled part were free surfaces, with the bottom surfaces as fixed constraints and the prescribed displacement applied to the top surfaces. The mesh was auto-generated by COMSOL using the 'extra fine' parameters, with the number of mesh vertices and elements varying with the geometry. The 2D models had an average over 50,000 elements, while the 3D model had over 650,000 elements. The prescribed displacement was generated by performing an auxiliary sweep from 0 to 0.18 mm with a step size of 0.02 mm. The properties of Ti–6Al–4V used in the simulations were taken from [60]. Within the damage subnode, the phase field damage model was used with elastic strain energy density as the crack driving force.

Results and discussion

Figure 1 is an optical image mosaic of a section of the sample, showing the presence of defects of different types throughout the sample, including LOF defects, spherical pores, and banding. The larger LOF defects are primarily located close to the edge of the sample (left side of the image). The spherical pores are of a length scale to not be easily observed in the mosaic image, but are resolvable in individual images. The bands that are perpendicular to the build direction (Z^+) throughout the sample appear as alternating dark and light adjacent 'linear' regions and are more easily distinguishable at the edge of the sample (left side of the image). Faintly in the background, features appear parallel to the Z-axis, and extend across many of the alternating light and dark bands. These share a directionality with columnar grains.

Banding

The alternating light and dark bands, parallel to the XY plane, observed in the optical micrographs (Fig. 1) showed no consistent thickness throughout the build height. The band thickness measurements ranged from 15 to 430 μm and depended on subjective visual determination of band location. These bands are not directly correlated with the programmed process layer thickness, which is 50 μm. Serial sectioning conducted on a sub-scale volume of the sample (i.e., one of the 1.5 mm × 1.5 mm × 12.5 mm 'toothpick' sub-volumes excised from the edge of the sample) was used to

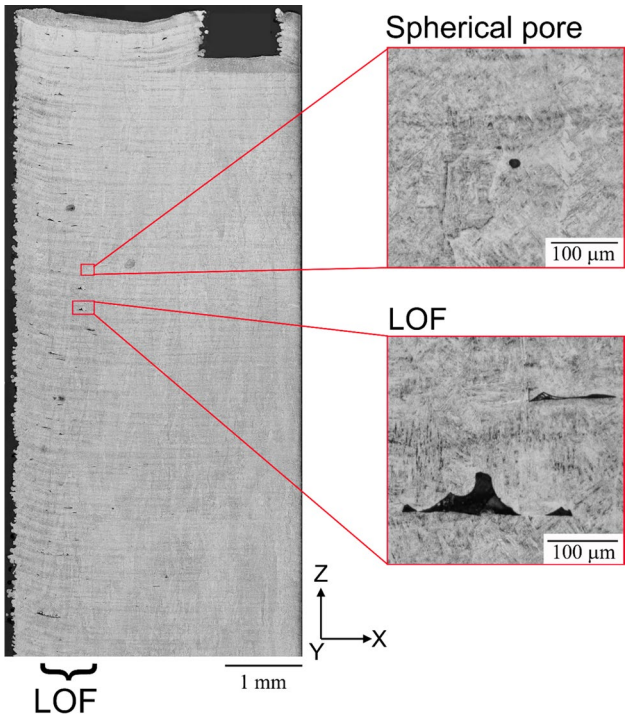

Figure 1 Optical mosaic of a portion of the sample showing banding (light and dark lines), spherical pores, and LOF defects throughout the build height. The right side of the mosaic is the centerline of the sample, as it was sectioned with electrical discharge machining from top to bottom, hence the straight line; the left side of the mosaic image is the edge of the sample where the superficial roughness of the electron beam melting process is observed. Note that the 'square' or notched cutout at the top right corner of the mosaic corresponds to the cross section through a sample ID label included in the print design. The region with the majority of the LOF defects is noted below the mosaic and extends throughout the build height (Z-direction). Magnified images of a randomly chosen spherical pore and a randomly chosen region with two LOF defects are shown

reconstruct these bands in 3D, and their reconstruction is shown in Fig. 2. During the reconstruction of the 2D optical microscopy data into 3D volumes, multiple steps are required. The first step involves image processing, in which the dark bands in every optical micrograph are segmented (Fig. 2a, b). This step is a manual process, as competing contrast mechanisms are present. Following segmentation, the second step involves the application of a materials science inspired image processing software (MIPAR) and its 3D toolbox to perform a 3D reconstruction of the segmented dark bands (Fig. 2c, d). Notably, the 3D reconstruction (Fig. 2d) showed that bands are consistently aligned with the XY plane (Z^+ is the build direction), strongly suggesting that the physics

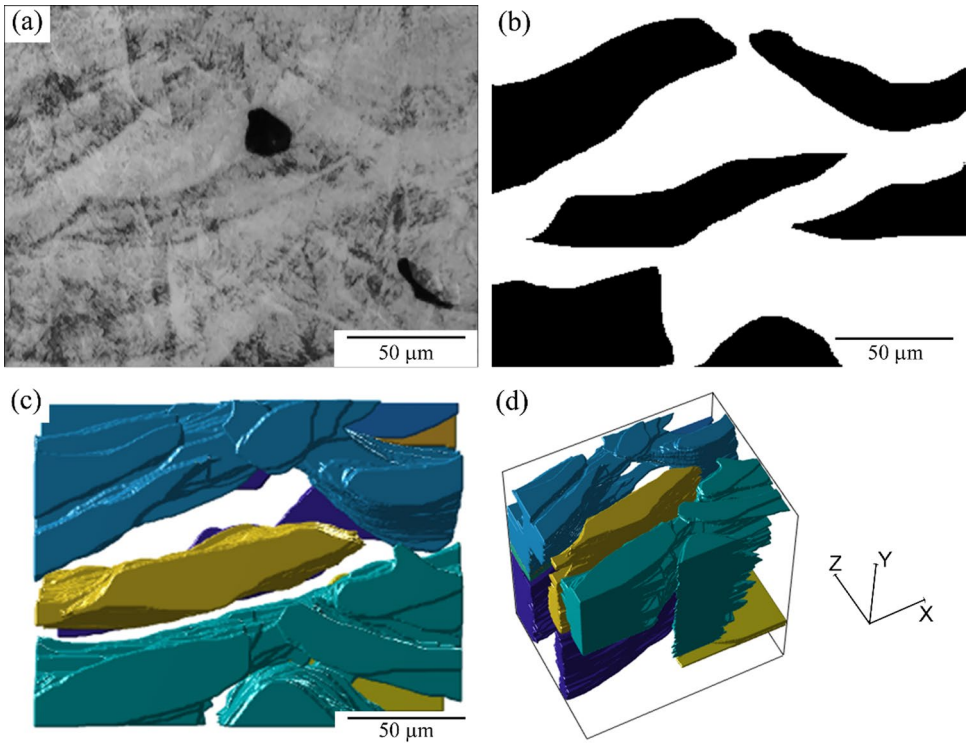

Figure 2 Banding observed in the samples: (**a**) optical micrograph showing banding and a lack-of-fusion defect formed between adjoining melt pools, (**b**) segmentation of dark bands (black color) and light bands (white) from the image shown in (**a**), (**c**) planar (XZ) view of the three-dimensional reconstruction of serial sectioning images of the dark bands showing this phenomenon (banding) as being a 'flat' and horizontal (XY) effect of the interactions and physics of melt pools, and (**d**) a three-dimensional view of the same reconstruction showing the flatness and continuity of the bands. For all (**a**), (**b**), and (**c**) images, the build direction is upwards

responsible for the banding act uniformly in the principal plane of the molten pool (mainly horizontal). The curvature observed at the edges/ends of the dark bands in Fig. 2b can be explained by melt pool morphology as two convex liquid pools come together, and are consistent with successive rasters with an elongated and trailing molten pool. As shown in Fig. 2a, the location where two melt pools make contact creates conditions where certain LOF defects can be formed, as the liquid material would need thermal energy to overcome capillary forces, fill the space, and wet/melt both surrounding material in the current layer and the previous one [61]. Causes for this banding phenomenon will be discussed in the next section.

Compositional fields and interaction with defects

Compositional analysis of the observed microstructural bands (Figs. 1 and 2a) using EDS showed that the bands represent spatial variations of composition in the as-deposited material (Fig. 3). The darker bands generally correspond to lower aluminum content, while lighter bands generally correspond to higher aluminum content. Subtle deviations from these general trends can exist due to local variations in the microstructure. Notably, the top most regions of the build, including the top (left-hand side of Fig. 1) and the notched region (upper left part of Fig. 1), represent the last volumes that were melted and solidified and are also darker bands. The pervasive variations in composition throughout the bulk of the build, and thus the banding phenomenon itself, are consistent with the preferential vaporization of aluminum from the surface of melt pools in vacuum environments [2, 62, 63] and the subsequent creation of volumes of liquids with different compositions and thus different densities and thermophysical properties. This solute differentiation, with a spatial variation, is responsible for the uneven nature of the bands. Similar effects

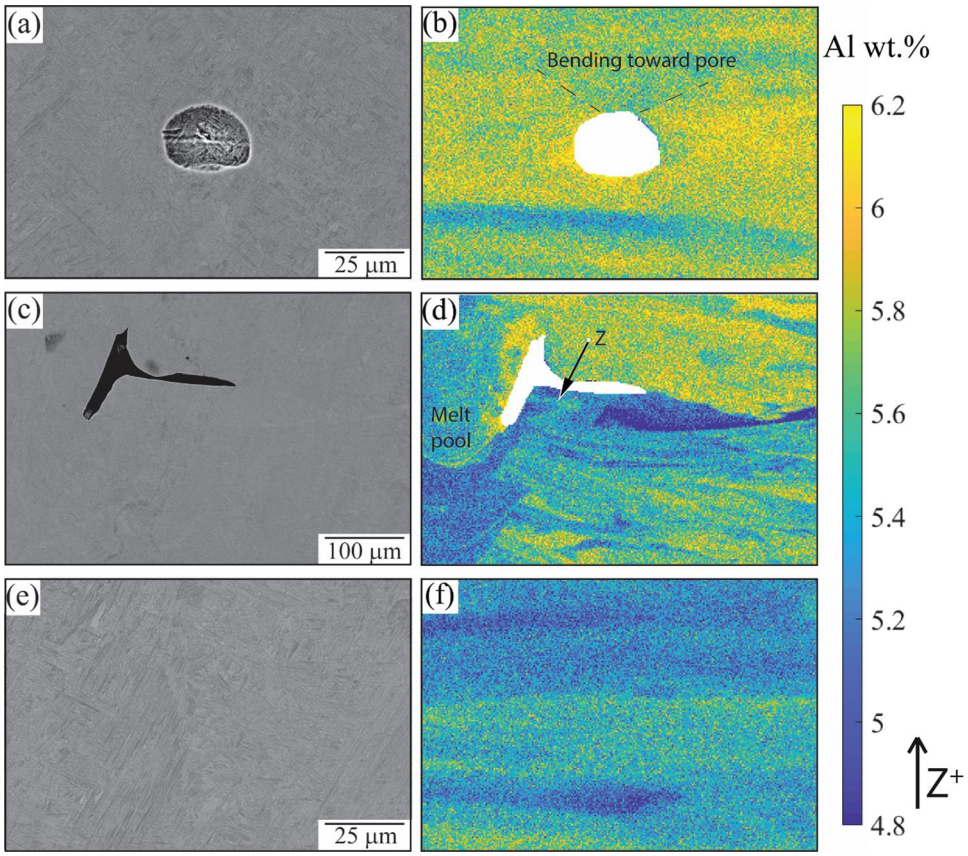

Figure 3 Compositional variations of bands. (**a**) back-scattered electron (BSE) image of a gas pore with its EDS map (**b**) showing low Al and high Al bands, (**c**) BSE image of a region surrounding a lack-of-fusion defect with its EDS map (**d**) showing variations in the Al content, and (**e**) BSE image of an area away from pores or LOF defects with its EDS map (**f**) also showing Al variations. The defect in (**a**) is from the top third of the sample, near the centerline; the defect in (**c**) is from the bottom third of the sample, near an edge; and the field of view pictured in (**e**) is from the top third of the sample a distance approximately 1/3 the sample's width from the edge

have been reported in other titanium alloys produced through AM methods [11, 64–66]. Given the expected effects of convection in AM processes, including both natural and Marangoni convection, the retention of this distinctive banding indicates that solidification proceeded faster than convective fields could redistribute (and mix) the different liquid compositions.

Figure 3a, b shows local, microscopic chemical variations surrounding a gas pore. The concentrations in the aluminum content on opposite sides of the pore are not symmetrical, with a higher concentration on the left side and lower concentration on the right side. Such an asymmetric variation hints at a phenomena associated with surface energies (e.g., Marangoni convection) where a pore may be dynamically coupled to a compositional fluctuation during fluid flow. In addition, the low Al band on top of the pore also seems to be interacting with the upper surface of the pore, further indicating a possible interaction due to capillary forces and fluid flow differences generated by the presence of complex compositional gradients, or less likely through a local mechanical contraction upon cooling. Figure 3c, d offers insights into the compositional variations surrounding LOF defects. There are four distinct features. Firstly, the shape of the defect might best be described as a 'sideways T,' indicating this is a complex 3D defect. As evidenced later in this paper, this is distinctly different from other more typical LOF defects which are constrained within a 2D plane. Secondly, the left quarter of the compositional map clearly shows evidence of the contour passes, whereas the right (3/4) of the map is of the raster scan region. Thirdly, there is a pronounced difference in Al above and below the horizontal portion of the defect. Lastly, there is a compositional 'zig-zag' as indicated by the letter Z in Fig. 3d, which indicates that the liquid convection in the molten pool was disrupted, likely here by the previously solidified contour pass. These features have been interpreted to propose a possible formation mechanism and evolution of this particular defect (see Fig. 4a–f).

In Fig. 4a, an arbitrary junction between the contour pass (left) and raster scan (right) presents the starting state. The next pass to occur would be a raster scan, which has stratified compositional bands. Upon interacting with the previous solidified contour pass, a portion of the stratified composition band is 'folded,' leading to the 'zig-zag' feature. Following another

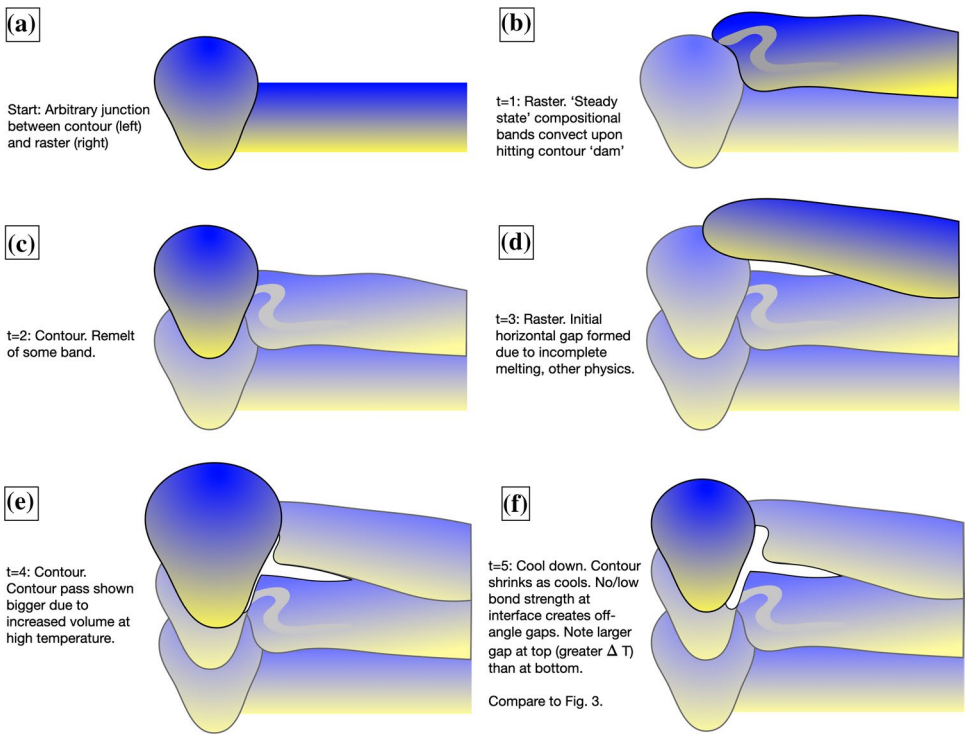

Figure 4 Schematic of evolution of the lack-of-fusion defect shown in Fig. 3c, d

contour pass (Fig. 4c), the next raster pass (Fig. 4d) experiences insufficient energy density[1] for complete melting, resulting in two interpretable 'fossils,' namely the in-plane (2D) lack-of-fusion defect and the greater overall Al concentration. The next contour, also experiencing a (likely) insufficient energy density, does not result in sufficient fusion below the surface (Fig. 4e). Upon cooling, the contour and raster will contract, resulting in an opening of the original lack-of-fusion gap (Fig. 4f).

Taken together, the interaction of the compositional fields with these defects gives the following insights. Both the prior passes and the defects (both spherical pores and LOF) interact with the fluid flow through various physical mechanisms, including, for example, geometric configurations where surface tension and capillary forces dominate, or at the very least play an important obstructing role during mixing of the heterogeneous stratified liquids in the melt pool generated by vaporization of elements, resulting in unique compositional signatures around defects. The Al concentration appears to be higher in regions that would be colder relative to adjacent regions. Notably, Fig. 3e–f shows Al-rich and Al-lean bands present in the sample in an area away from any defects. These bands appear flatter and more uniform than those observed surrounding pores and fewer ripples (or turbulence) are observed, supporting these insights into the interactions of defects and bands.[2] The data also indicates that compositional variations are not affected once the material has solidified, i.e., solid–solid phase transformations do not alter these mesoscopic compositional variations. This observation is not surprising, given the solid-state kinetics and relatively large diffusion distances. Banding can thus be related to aluminum vaporization upon initial melting, or during subsequent cycles which raise the temperature enough to induce further melting and vaporization, and not during subsequent thermal cycles that do not exceed the liquidus and only contain solid–solid

[1] Of note, the interpretation of insufficient energy density is of the total local available energy density, comprised of the beam energy, the thermal mass of the deposition, any perturbations in local heat transfer, and the mass of material to be melted.

[2] This observation of extended compositional fluctuations around defects is novel and may provide new methods of identifying and interpreting defects using nondestructive evaluation techniques [18, 19, 67, 68], as the volume of distinctively different material is larger than the pore. Although banding has previously been observed, to the authors knowledge, the interactions of composition with defects have not been reported in the literature.

thermomechanical gyrations [42, 62, 69, 70]. Notably, these spatial variations in Al concentrations will alter the liquidus, and thus, local variation in melting/solidification may occur.

More unique compositional features beyond simple horizontal banding reveal information about fluid flow within melt pools which may be more related to solute segregation following initial vaporization. The concentric ripples observed in the presence of spherical pores (Fig. 3b) and unique variations such as the Z-shaped region of relatively higher aluminum content under the LOF defect indicated with an arrow in Fig. 3d suggest that the fluid flow within the molten pool plays a larger role in the compositional variation phenomenon than previously thought. Given the length and time scales at which melting and solidification processes occur during AM, especially when the heat source rasters across a powder layer, surface tension effects (i.e., Marangoni convection) are responsible for much of the fluid flow within the melt pools [1, 21]. This fluid flow has the largest effect on pore formation and entrapment for spherical porosity [12]. The forces associated with buoyancy and gravity are also present in melt pools but can often be disregarded as they have a negligible effect compared to the influence of surface tension [21, 71]. As the melt pool cools, drag becomes the dominating force [12, 21, 72]. The conjunction of these fluid flow forces with the presence of defects is also responsible for exacerbating ripples and turbulent signatures ('fossils') not observed in regions without defects. Notably, the kinetics of solidification must occur on a time scale that prevents large-scale mixing, allowing for the creation of such compositional features in the final build as post-build static informants. Examining compositional fields in regions around defects, including larger LOF defects which will have a greater impact on fluid flow, can thus be used to delve into the fluid flow of melt pools as well as give insight into the kinetics of solidification, given the high thermal gradients and fast cooling typical to AM processes.

The significance of the compositional variations and their influence on the resulting materials state, locally and globally, can be considered by particularly examining the influence of aluminum on the properties of the alloy. Firstly, Al has a strong influence on the β-transus temperature of Ti–6Al–4V. With local variations in composition of over 1wt% in some regions, any heat treatment or thermal process that hovers near the β transus will thus result in different effects in the differing compositional regions. Secondly, Al has a strong influence on the mechanical properties of the alloy as well, as shown previously by [73, 74]. Using the work of Hayes et al., and keeping all other variable values equal, aluminum concentration x_{Al} can be directly related to the yield strength of the material [74]:

$$\begin{aligned}\sigma_{ys} =& 89F_V^{\alpha} + 45F_V^{\beta} + F_V^{\alpha}\left(149x_{Al}^{0.667} + 759x_O^{0.667}\right) + F_V^{\beta}\left(\left(22x_V^{0.7}\right)^{0.5} + \left(235x_{Fe}^{0.7}\right)^{0.5}\right)^2 \\ &+ 150F_V^{\mathrm{col}}\left(t_{\alpha-\mathrm{lath}}\right)^{-0.5}\left(t_{\beta-\mathrm{rib}}\right)^{0.5} + 125F_V^{col}\left(t_{\mathrm{colony}}\right)^{-0.5} - \mathrm{AxisDebit} + F_V^{BW}\alpha MGb\sqrt{\rho}\end{aligned} \quad (1)$$

where x_i is the weight fraction of element i in the alloy, F_V^i is the volumetric phase fraction of either phase (α/β) or microstructural feature (colony-col/basketweave-BW) i, t_i is the thickness of feature i, *AxisDebit* corresponds to the texture debits (easier slip), and $\alpha MGb\sqrt{\rho}$ is the Taylor hardening equation. As compared to the nominal composition (6wt% Al), a small loss of 0.2wt% Al would lead to a decrease in yield strength of ~ 2%. A more significant loss of a further 1wt% Al (down to 4.8wt% Al) would lead to a decrease in yield strength of ~ 14%. Beyond using compositional fields to reveal information about AM processes, they must also be considered when assessing the final materials state of parts.

Lack-of-fusion (LOF) defects

LOF defects themselves have a preferential location relatively close to the edge of the sample (Fig. 1) but with a 'healthy skin' between the defects and the edge. The skin is the direct result of the contouring deposition pass that was performed before each layer was deposited using a raster scan fill strategy. The LOF defects appear in a manner that has been described as chimney-like [75], as they are located through the entire build height (Figs. 1 and 5), from bottom to top, and in the same approximate XY location in every layer. X-ray CT data (see Fig. 5) reconstructed using the MIPAR 3D toolbox show that these defects are relatively flat with major axes in

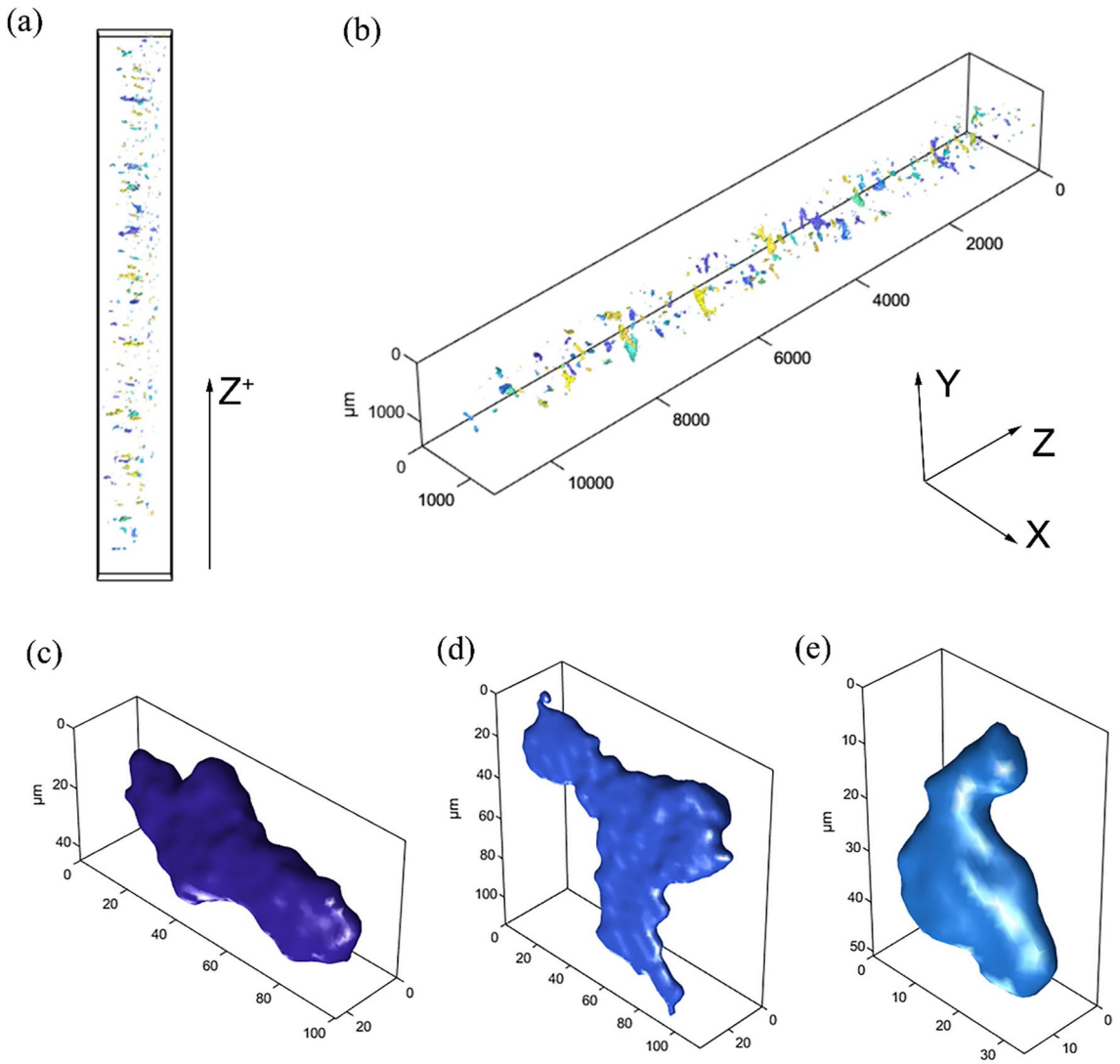

Figure 5 Reconstructed 3D LOF defects from an X-ray CT scan of a stick sub-sample excised from the edge of the build: side (**a**) and isometric (**b**) views. (**c**–**e**) Examples of defects with diverse shapes and sizes, but which are all flat (XY direction). Subfigures (**b**), (**c**), (**d**), and (**e**) have the same 3D orientation

the horizontal (XY) plane (Fig. 5c–e) and a relatively small height (Z-axis). The morphology strongly supports the hypothesis that these defects are the result of a melt pool not being able to wet and/or melt the previous layers, creating local gaps between layers. The mechanism may be similar to that shown in Fig. 4c–d, where the liquid raster interacts with the contour in a way to create these LOF defects. The preferential location of LOF defects is correlated with programmed changes in the power and the velocity of the electron beam decelerating near the edge before turning around and continuing the next pass, with the beam providing less energy to the material and thusly changing the wetting and thermal properties of the melt pool. These results, coupled with other results where the power and velocity are not changed thereby leading to spherical pores forming as a result of a dominant keyhole mode [76, 77], indicate that the balance of power and velocity is critically important in these locations and that there is still a need to optimize the balance to not only avoid spherical porosity formation due to excessively deep keyholes [31], but also the formation of these lack-of-fusion defects shown here.

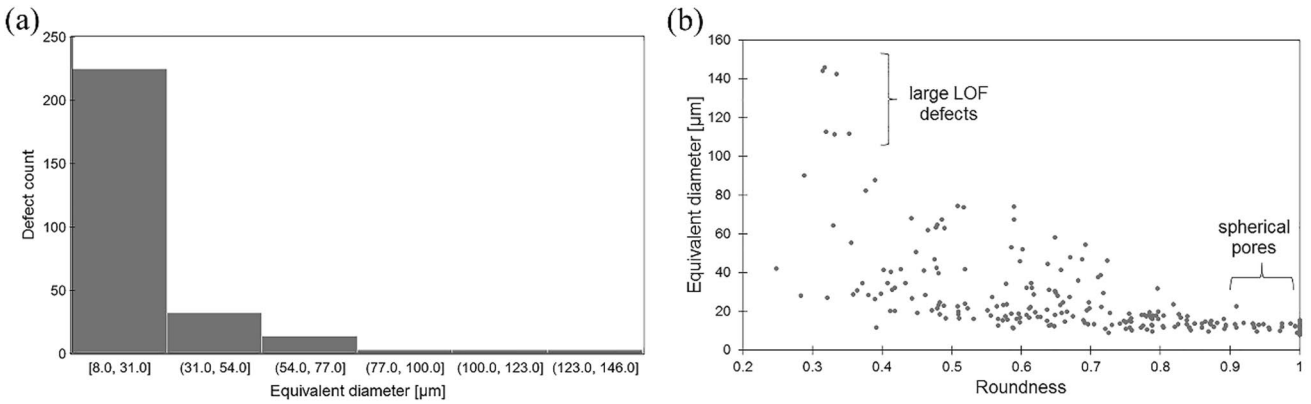

Figure 6 Distribution of defect measurements from the reconstructed 3D data of Fig. 4. Data displayed is (**a**) distribution of equivalent diameter and (**b**) roundness versus equivalent diameter, showing a cluster of lack-of-fusion pores and a tail end of very small and very circular pores. Roundness values close to 0 represent flat and elongated ellipses. A value of 1 represents a circle

Extrapolating from the X-ray CT data, considering the resolution of the technique (anything < 432 µm^3 is not resolvable[3]) and working on the assumption that almost all lack-of-fusion porosity is limited to the edges of the sample with only a few exceptions (as observed from optical micrographs and mosaics such as Fig. 1), the volume fraction of LOF defects in the full build (15 mm × 15 mm × 25 mm) would be close to 1.51×10^{-4} (0.0151%) distributed in approximately ~ 10,000 defects of different sizes (average equivalent diameter to a sphere of 23.8 µm with a standard deviation of 22.1 µm) [58, 78]. The largest defect that was observed and measured in CT had dimensions of 111.7 µm × 369.5 µm × 651.1 µm. The majority (~ 80%) of the pores (Fig. 5a and b) have equivalent diameters < 30 µm. The roundness (measured in their XY plane) of defects ranges from 0.2 to 1, with an average of 0.7, where a roundness value of 0 would be a straight line, and a value of 1.0 would be a perfect circle [78]. As presented by Wolff et al. [79], pores with a higher roundness value (more circular) can be related to lower cooling rates (0–500 K s^{-1} for directed energy deposition AM Ti–6Al–4V), while less round pores can be related to higher cooling rates (> 1500 K s^{-1}). Pores with higher roundness value approximate spherical morphologies and can be a result of keyholing [72] or entrapped gases [11], in raster scan strategies. The Ti–6Al–4V material presented in this paper has been analyzed previously, and gas pores of an equivalent size have been identified in the virgin powder prior to deposition [11]. Figure 6 shows the distribution of equivalent diameter and roundness. Spherical pores, defined as those defects with a roundness of 0.9–1.0, only account for 30% of the total dataset. However, the analysis shows that there exists a small cluster of large defects (110–150 µm) with a roundness of ~ 0.35 (considerably below the average).

During the application of these materials, the knowledge of the distribution of defects, particularly the larger LOF defects that can be present in AM processes, can be used in the determination of potential failure mechanisms. The effect of defects on the mechanical behavior of the part is a complex problem that requires the consideration of the size and shape of the defect, proximity of neighboring pores, geometry of the part, location of the defect in the part, possible thermal gradients (cyclic due to the AM nature of the process), processing parameters (e.g., type of AM, material, power, dwell time/beam speed, layer height), and the number of features overall, among other factors. A full physics modeling and simulating effort to study the influence of all of these factors individually, as well as in combination, would be beneficial in understanding the role they play in the resulting mechanical behavior, but this would likely require a more complex structural mechanics approach, including potentially linking in crystal plasticity, and is thus beyond the scope of this paper. However, simplified models of damage considering ellipsoid/ellipse voids, to represent large LOF defects,

[3] This number comes from a ± 2pixel resolution of the X-ray CT dataset scaled into the dimensions of the sample 6 µm x 6 µm x 12 µm.

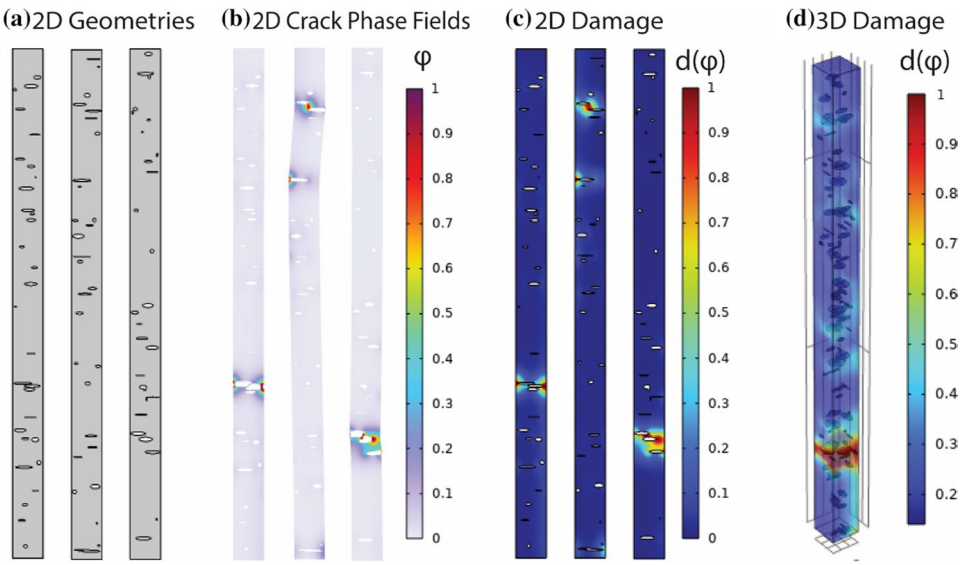

Figure 7 Finite element simulations of cracking (brittle behavior modeling) of Ti64 models with defects. (**a**) 2D geometries of three models with 30 randomly generated ellipse defects in each one of the 1.5 × 25 mm rectangles, changing the size and location of the defects in each; (**b**) crack phase fields, plotting φ, after identical applied tensile forces to the three 2D models shown in (**a**); (**c**) damage fields d(φ) after identical applied tensile forces to the models shown in (**a**) and (**b**); and (**d**) the damage field after an applied tensile force to a 3D model with 100 ellipsoid defects

were used to show the influence of defects on damage fields after being subjected to tensile forces. The geometry and position of the defects was randomly generated in COMSOL and based on experimental results (sizes and shapes) of the previously presented CT data, meant to represent a 'worst-case' scenario, such as the region high in porosity at the edge of the sample. Considering the distribution and number of large defects detected through X-ray CT, for 2D models, 30 ellipses were thus introduced to a 1.5 × 25 mm geometry; while for the 3D models, 100 ellipsoids were introduced to a 1.5 × 1.5x25mm geometry (same size as the sample shown in Fig. 5a, b).

The 2D models (Fig. 7a–c) were exercised for multiple geometries to better elucidate the influence of the defects. Each 2D model was executed with the same materials properties and model conditions; only the defect geometry (i.e., the placement and size of the ellipse defects) was altered. Extending the modeling to 3D (Fig. 7d) reveals similar results. Phase field modeling, as shown through the crack phase fields in Fig. 7b, is an extension of the Griffith fracture theory and models crack propagation through scalar fields [80]. The *damage* variable output in COMSOL (Fig. 7c, d) represents the amount of deterioration due to crack growth. This damage evolution function, unitless, can be modeled by:

$$d(\varphi) = 1 - (1 - \varphi)^m \tag{2}$$

where d is the damage variable as a function of the crack phase field (φ) and m is a coefficient whose value represents the parametrized degradation, $m = 2$ for quadratic (as was the case shown in Fig. 7c, d), $m = 3$ for cubic, etc. [81–83]. The crack phase field (φ) is a function of stress (σ), elastic modulus (E), and strain (ε) as follows [81]:

$$\varphi = \sqrt{\frac{\sigma}{E\varepsilon}} \tag{3}$$

In some models, the crack phase field and damage variables remained at or near 0 excepting a single region where the crack occurred, showing a high preference for a local stress concentration. In other models, such as the center of the three 2D models shown, multiple regions throughout the model led to stress concentrations and/or cracking. The degree of cracking is indicated in both the crack phase field and damage variables (Fig. 7b–d), with regions nearest the cracks experiencing values greater than 0.3, with 1 being the maximum possible value and an indication of the crack location(s). In both the 2D and 3D models, the regions of highest damage were not

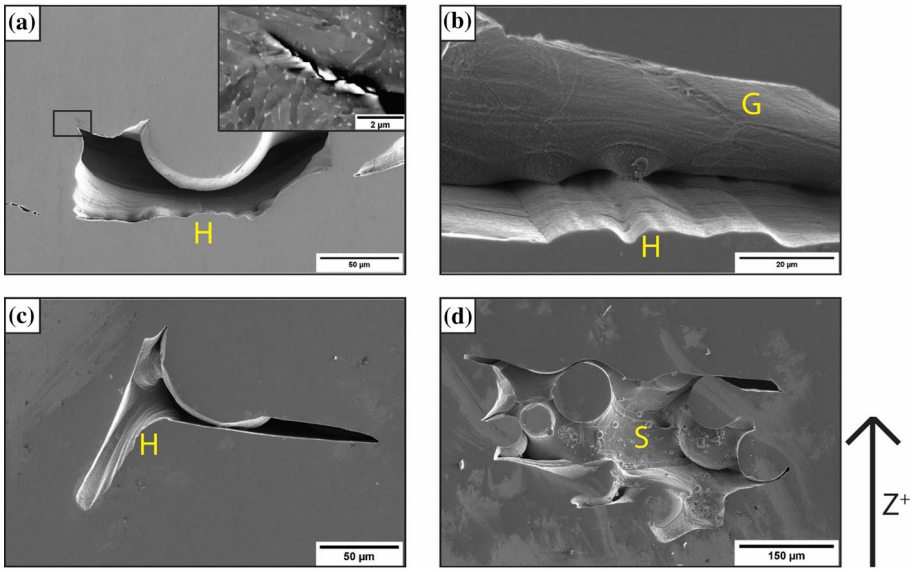

Figure 8 LOF defects with different characteristics: (**a**) an overhanging/partially melted powder particle and fluid flow (humping [H]) on the 'floor' of the cavity, and a crack on the upper left side of the defect with a magnification of this region in an inset; (**b**) humping [H] (lower part of the defect) and microstructural relief including thermal grooving [G] (ceiling and back wall); (**c**) a defect with very acute angles in the top and right tips acting as stress concentrators, and fluid flow evidence [H] on the wall, floor, and ceiling; (**d**) a larger LOF defect which extends through more than a single build layer (i.e., > 50 µm in height) showing spattering [S] and solid-state transformations (microstructural relief) in the back wall. The defect in (**a**) is from the bottom third of the sample, a distance approximately 1/3 the sample's width from the edge; the defect in (**b**) is from the bottom third of the sample, a distance approximately 1/3 the sample's width from the edge; the defect in (**c**) is described in Fig. 3; and the defect in (**d**) is from the bottom third of the sample, approximately 4 mm in from the sample's edge

only those regions which had defects close to the edge of the sample, but those which had multiple defects present in their vicinity.

Lack-of-fusion defects in AM can be a result of several mechanisms, which often interact with and compete against each other [44, 84–86]. The morphology of LOF defects can lead to additional detrimental features as well, such as the crack shown propagating from the upper left corner of the defect in Fig. 8a and inset. When considering the finite element simulation of ellipsoids above, in addition to the size, shape, and proximity of defects, uniaxial tensile loads or cyclic loads (i.e., fatigue) can exacerbate cracking initiated in sharp corners of the LOFs [49, 50].

Figure 8b shows crests and valleys on the floor of the LOF defect, known as humping transition or simply humping, formed as a result of instabilities of the melt pool due to surface tension effects in combination with backward fluid flow [86–89]. These capillary instabilities are known to be caused by low energy input from the electron beam [86, 87]. Another LOF in the same general region (Fig. 8d) experienced another phenomenon caused by low energy input, spattering. Spattering is the term for small, melted spheres ejected or spattered from surrounding melt pools [86]. If the spattered particles are large enough, they can create topological surfaces (XY plane) resulting in unevenly spread powder (different amounts of powder in different locations of the layer). However, in the case shown in Fig. 8d, the presence of spattering can be used to create a timeline for the formation of different defects. To observe spattered material on the walls of a LOF defect means the defect was already formed (or at least this wall of the defect was already formed) when the spattered material was ejected from surrounding melt pool(s). A schematic for the evolution of this defect with spatter (Fig. 8d) is shown in Fig. 9.

Void free surfaces, microstructural relief, and thermal grooving

The internal free surfaces of LOF defects can also show evidence of fluid flow (Fig. 8a, b), hinting at the time period these defects spend at elevated temperatures. Figure 8b and d shows indications of the solid-state

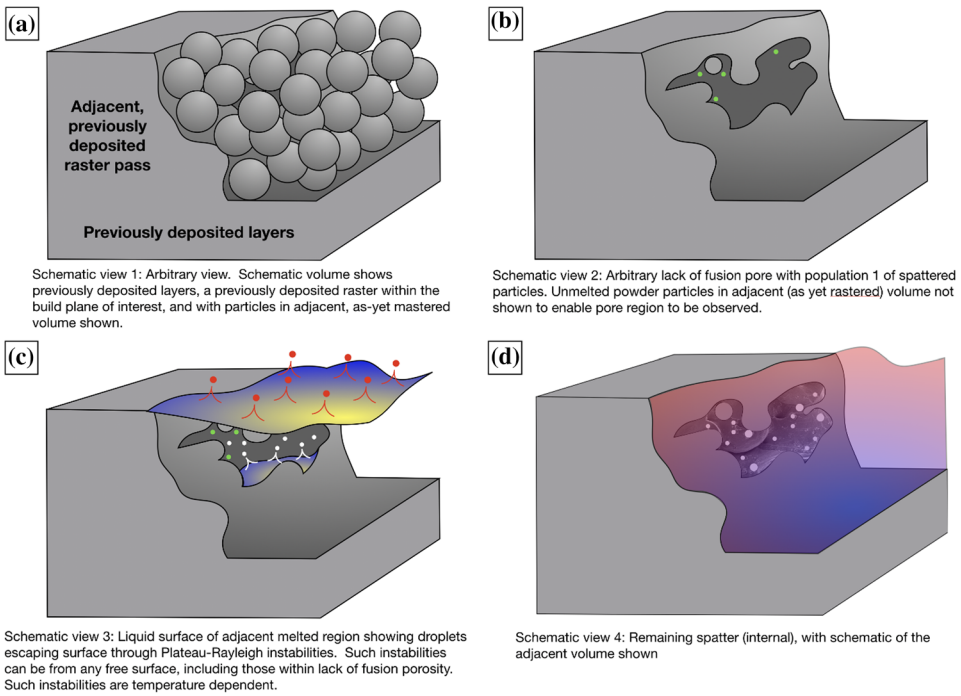

Figure 9 Schematic showing the evolution of a pre-existing lack-of-fusion defect from one raster path to then contain spatter. The spatter may exist from its initial formation, but is also likely to form due to the melt pool dynamics of the adjacent raster

transformations known as microstructural relief (see 'ceiling' of Fig. 8b and 'back wall' of 8(d)), which reveal information about which mechanisms of formation are at play and the timeline formation of these features.

Analysis on the internal free surfaces of defects can be used to deduce some details of the local thermal history. A series of experiments on powder particles were conducted to study the effects of temperature for identical hold times (above and below the β transus). The initial step in this particular mini-experiment was the imaging of both virgin (i.e., powder in its as-received state, before AM or sintering experiments) and used (i.e., powder extracted from the AM build chamber after the samples were printed) powder. Virgin powder (Fig. 10a, b) showed a combination of smooth surfaces along with impact-deformed surfaces (with plates, similar to tectonic plates, protruding and with evidence of movement after impact by a smaller and presumably solid, colder, and harder powder particle). The particle size distribution fits the reported 45–105-µm-diameter distribution from the supplier, with smaller satellite particles present (Fig. 10a, b). A small fraction of the powder particles had oblong or non-spherical shapes (Fig. 10a). Used powder (Fig. 10c) recovered from the AM system, conversely, showed clear evidence of microstructurally induced surface relief, as α-laths form/evolve and protrude from the surface (similar to tenting [90, 91]), suggesting that even though these powder particles may not have been in direct contact with the electron beam, the temperature in the chamber was still high enough to activate these microstructurally induced surface-relief-related phenomena.

The virgin powder was then subjected to temperatures above and below the β-transus. Powder sintered below the β transus (925 °C) (Fig. 10d) showed surface relief unrelated to the final $\alpha + \beta$ microstructure, as opposed to the α laths clearly seen on the surfaces of the used powder (Fig. 10b). Powder sintered above the β transus (1025 °C) (Fig. 10e) showed the same type of surface relief as well as thermal grooving, which is a result of the prior β grains which existed before cooling to the final microstructure [92]. Thermal grooving occurs at elevated temperatures for grain boundaries that intersect the surface of a polycrystalline material [92–94]. There are several mechanisms of formation for thermal grooves, including evaporation and condensation or surface diffusion, as well as a modification of the dihedral angle to minimize the grain boundary-free surface triple junction. The conditions for the sintering experiments (time at temperature, inert gas atmosphere) compared to observations in the AM samples indicate that surface diffusion is a likely mechanism for these samples [92, 93]. Ten fields of view were evaluated for both sets of sintered powder.

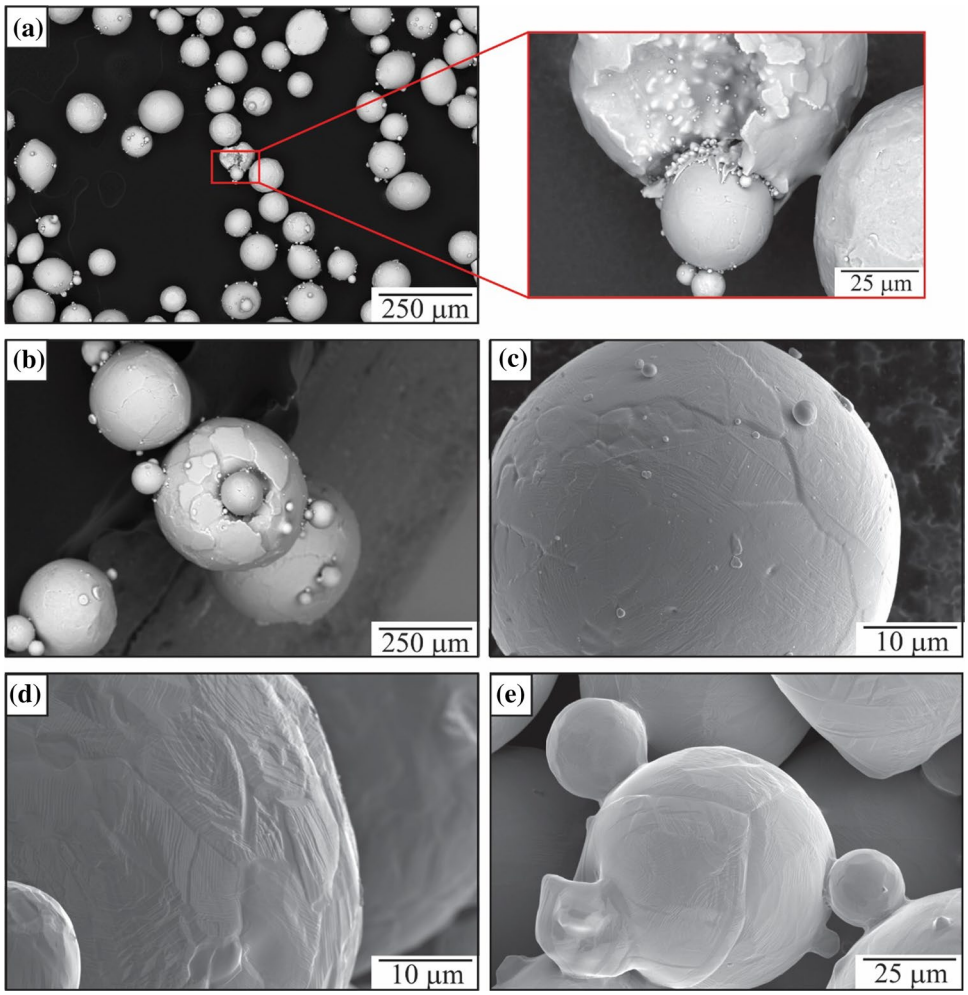

Figure 10 Surfaces of powder particles observed in the SEM: (**a**) virgin powder, showing the general particle shapes and sizes, with a subset showing a combination of smooth and impact-deformed surfaces, satellites, and a small particle that impacted a larger one creating deformation of the surface similar to tectonic plates; (**b**) virgin powder, showing a powder particle with satellites as well as the impact of another, smaller power particle; (**c**) used powder, showing microstructural relief (α laths on the surface) and spattering of material ejected from melt pools; (**d**) virgin powder sintered at 925 °C, showing surface relief; (**e**) virgin powder sintered at 1025 °C, showing surface relief and thermal grooves

No thermal grooves were observed in any particles imaged from the powder sintered below the β transus. Of the particles imaged from the powder sintered above the β-transus, 174 particles were analyzed and 29 of them (or 17%) were found to contain thermal grooving. Similar thermal grooves were also seen in LOF defects, indicating similar locally activated thermal processes following grain formation. The defects that contained thermal grooves were found throughout the build height; however, identification of thermal grooves was largely dependent on the visibility of interior surfaces (both walls and ceilings) of the defects analyzed, which is limited due to the complex morphology. Within a single 15 mm × 25 mm (YZ) plane, 21 LOF defects were assessed, with 9 of them having features consistent with thermal grooves. In other words, these experiments confirm that the portions of the build surrounding the defects were exposed to temperatures above 1025 °C long enough for thermal grooving to take place, but short enough to limit grain growth. However, more in-depth approximation of the temperature at which such defects were held, as well as the time held at that temperature, would require additional high-precision in situ measurements of surfaces of the defects in question, an exceptionally difficult if not impossible experiment to conduct currently.

Spattering, cracks, and grain growth through defects

In addition to the structures on the free surfaces of LOF defects, other features also provide information about the AM process. Lack-of-fusion defects were observed to contain both cracks and spattered particles. The presence of spattering (Fig. 11a) occurs when small blobs and droplets of liquid metal are ejected from the melt pool as it is interacting with the electron beam [86, 95] and can reveal information about the

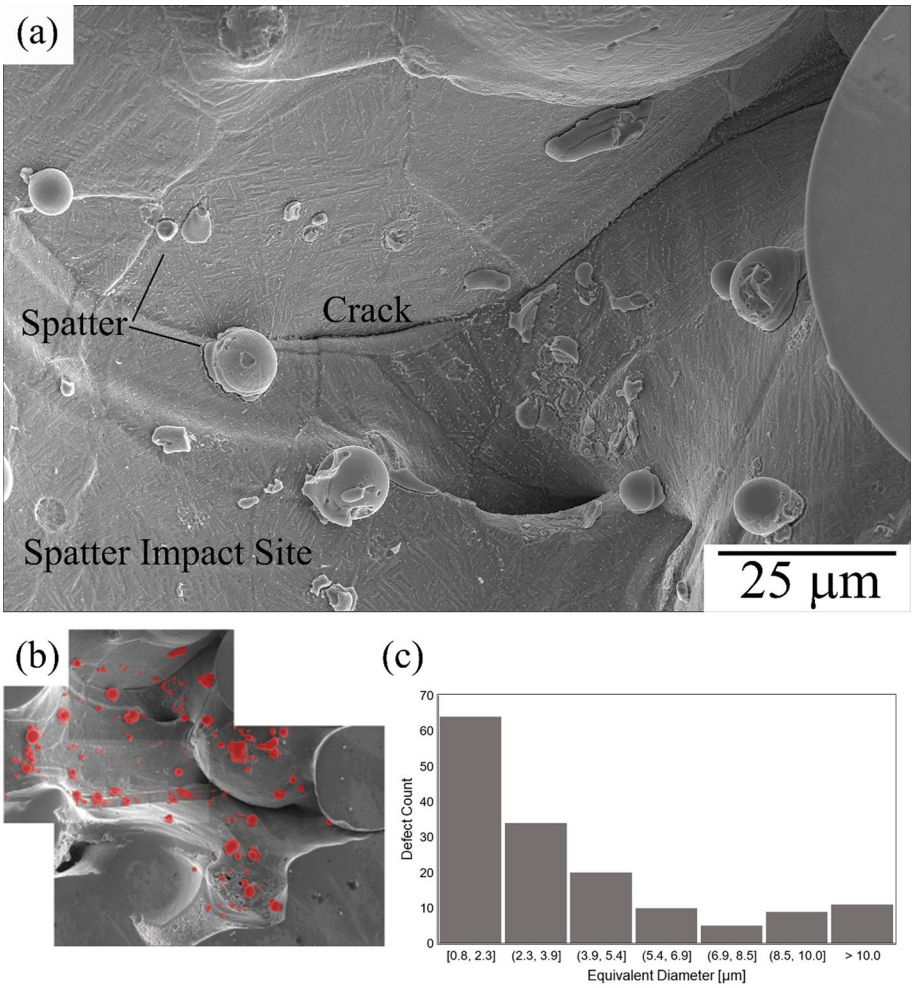

Figure 11 LOF defect (shown in Fig. 8d) with the following characteristics: α laths distinguishable on the surfaces, (**a**) crack formed between the 'walls' and the 'ceiling,' spherical particles (spattering) ejected from a nearby melt pool and subsequently landed on the already formed surfaces that underwent the β transus microstructural transformation, and is an imprint of a spattered particle that fell from the wall (lower left corner); (**b**) collage of BSE images of the defect shown in Figs. 8d and 11a with identified spattered/ejected particles shown in red; and (**c**) distribution of equivalent diameter of ejecta from (**b**)

timeline of characteristics observed in LOF defects, as it is logical to assume that the internal surfaces of the defect must have existed prior to these droplets landing and sticking to the walls. These droplets can land anywhere, from already solidified contiguous material, regions of the melt pool (where they may become reintegrated due to wetting and capillary forces), or onto walls, floors, and ceilings of nearby volume defects such as pores or surfaces of lattice structures [86, 95], or here, on an adjacent, previously processed raster path. Furthermore, α-laths can be seen on the surfaces of the LOF defect while the spattered particles are generally smooth. Finally, there is an impression of a spattered particle that detached from the wall in the bottom left corner of Fig. 11a with α laths distinguishable inside the imprint. Taken together, along with the less pronounced thermal grooves on the bottom and absent thermal grooves on the side and top walls, suggest that this defect had a colder overall thermal history.

Considering this LOF defect as a metallurgical fossil record, the spattering phenomena can be analyzed further. These ejecta spatters were analyzed using MIPAR image analysis software, and the identified ejecta are shown in the SEM micrograph montage (Fig. 11b). Statistics of the ejecta observed and measured in this LOF defect show that the more than 40% of all spattering events result in small particles (sizes smaller than 2.3 μm; recall the given powder particle size ranges from 45 to 105 μm) landing on already formed surfaces (in this case, the floor, walls, and ceiling of the LOF defect). While in situ techniques, such as high-speed, high-energy X-ray imaging, can detect ejected particle sizes and trajectories during AM processes [96, 97], smaller particles are thought to have the ability to be reintegrated into melt pools, making post-deposition detection and characterization difficult, if not impossible, except through these types of metallurgical fossil records such as the LOF defect shown in Figs. 8d and 11a. Some particles retain what appears to

be partially spherical shapes, though due to the three-dimensional topographical nature of the surface of the defect and the ejecta, and the fact that SEM imaging is a two-dimensional observation, the actual shape of the ejecta is an approximation.

Subsolidus weld cracking, which shares similarities with the cracking observed in Fig. 11, has been associated with a loss of ductility, and specifically for Ti–6Al–4V with a higher fraction of colony microstructure [98]. In general, higher cooling rates result in a microstructure with a higher volume fraction of basketweave (and thus less colony) [98], assuming that the composition does not change.[4] In Ti–6Al–4V AM processes, if the parameters are not carefully selected for the design of the part, the bottom section would contain the highest basketweave fraction since it is in contact with the base plate (kept at a constant temperature, lower than that of the build chamber), while the middle and top regions would develop a mix of basketweave and colony [104]. The fraction of basketweave and colony can even reach a steady-state after a certain height [13]. With all else being equal, basketweave volume fraction measurements (as reported in [13]) are as expected considering that electron beam rastering induces high basketweave formation due to their higher cooling rates [11, 26, 105], with the highest fraction observed at the bottom of the sample (~ 1 mm; 98.2%) since it is in contact with the steel base plate. Given the high volume fraction basketweave, cracks that form within defects (Fig. 11) are unlikely to be a result of subsolidus weld-induced cracking. In addition to generation local thermal gradients, the geometry and volume of the large LOF defect (Fig. 11) lead to morphological stress concentrators and crack formation.

The EBSD map shown in Fig. 12a can reveal information about microstructural changes as a result of the AM build parameters and the presence of defects. To aid in the interpretation of these results, parent β grain reconstruction (Fig. 12b) using the MTEX Toolbox in MATLAB has been used to highlight the interaction of defects and grain growth. Firstly, as expected in AM parts [13, 106–110], the nominal build direction (Z-axis) and the columnar growth direction are not perfectly parallel, as there is a slight tilt of the growth axis to the left (for this map) as a result of the beam (and energy) rastering in the XY plane, creating thermal gradients that are not aligned with the z-axis. Secondly, the presence of overhanging partially melted particles, like the one shown in defect 1 from Fig. 12a (and Fig. 8a), can nucleate small grains, and will have an influence on the local texture. Particles suspended from the ceiling of LOF defects have different local thermal conditions when compared to continuous columnar grains. The normal melt pool now interacts with a thermal barrier (in the form of the lack-of-fusion defect) which prevents the melted material from reaching the material below. Such defects also prevent vertical heat transfer, and a solid powder particle insufficiently heated results in the particle partially retaining its original shape, with only a portion melting and interacting with the rest of the part. Further examples of this can be observed in defects 3 and 4 (Fig. 12a). The interrupted heat transfer allows these overhanging powder particles to act as new nucleation sites, promoting the formation of new grains. An example of this can be seen at the left edge of defect 3 (Fig. 12a, b). Thirdly, elongated LOF defects can play a role during the columnar growth of parent β grains, as evidenced by two clear examples from Fig. 12b. Examining defect 3 showcases the parent β columnar grains below defect 3 stopping at the 'floor' of the defect while new β grains (with different orientations) start their growth at the 'ceiling' of the LOF defect and continue growing until encountering another defect.

Considering defect 2, the results are more interesting and complex. In the region surrounding this lack-of-fusion defect, portions of the microstructure show a nearly identical orientation both above and below the defect for some, but not all grains. For example, prior β grains 7 and 8 share a nominally identical grain width and might appear continuous, but they have distinctly different orientations. Conversely, for the group of grains (11, 12, and 13) on the right end of LOF defect 2, the grains labeled 12 and 13 are nearly indistinguishable in their orientation, while 11 is different. Grains 9 and 10, as well as grains 5 and 6, have identical orientations both above and below the LOF defect. These similarities, particularly away from the ends of LOF 2, may appear anomalous. Figure 13a–d shows backscattered SEM images of the defect at $a \pm 25°$ equivalent

[4] In Ti–6Al–4 V, α stabilizers promote colonies, while β stabilizers promote basketweave [99–103].

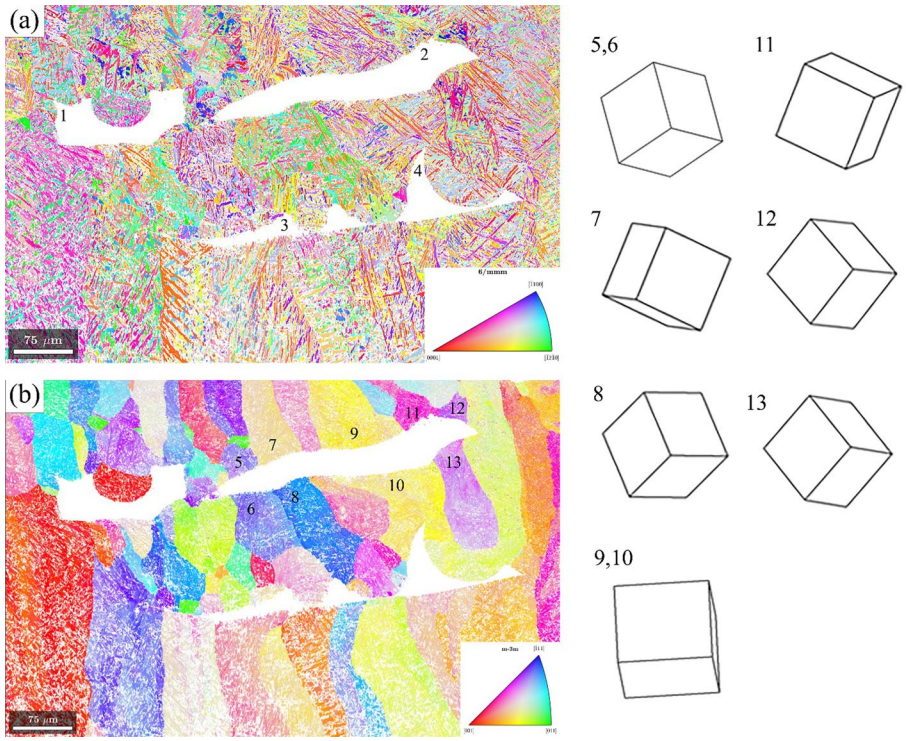

Figure 12 EBSD maps of the area surrounding LOF defects. (**a**) Inverse pole figure plot of α phase, (**b**) parent β grain reconstruction, and three-dimensional orientation of selected prior β columnar grains shown on the right side. The LOF defect (1) shown in the upper left portion of the image is the one shown in Fig. 7a. Distinct LOF defects in (**a**) and distinct prior β columnar grains in (**b**) are labeled

tilt.[5] These images provide some critical information. Firstly, features associated with microstructural transformations (the formation of the hcp alpha laths [111]) and the prior β grain boundaries can be observed. Of brief note, the subtle phase transformation 'tenting' is more apparent on the 'top' of the LOF defect, while the grain boundaries appear to have some signatures of deformation (grain boundary sliding/extrusion) on the 'bottom' of the LOF defect. Secondly, when both Figs. 12 and 13 are critically analyzed together, the orientation data can be mapped with the grain boundaries. There are two types of grains: those that are crystallographically continuous (C) across the LOF defect, and those that are not continuous (NC). Each continuous grain (except 12 and 13, which are not clearly seen in Fig. 13) can be observed to be continuous on the *back* of the LOF defect (i.e., there are no grain boundaries between the polished EBSD surface and the back of the pore). Reasonably, grains 12 and 13 can be assumed to be continuous either in the back of the pore (which cannot be seen) or on the front of the pore that was polished through. Figure 14 shows a schematic of the possible formation of this defect, showing the continuity of some grains but not others. Thus, the three-dimensional nature of the microstructure (including defects) is associated with grain continuity around the defect. This grain continuity has an important consequence. As the solidification proceeds *around* the defect, rather than necessarily nucleating on the suspended liquid surface, it gives insights into the fact that grain growth is preferred over nucleation. Further, the thermal gradients around the LOF defect may *strongly* deviate away from the Z-axis.

Conclusions

Defects in AM parts, while undesirable under many application conditions, can be useful to understand the physical processes and mechanisms acting during the different stages of the manufacturing process, as well as the order with which they operate in a build. This work proposes different ex situ techniques to analyze pores, LOF defects, banding, and chemical composition variations observed in a rastered e-beam AM sample, with the ultimate goal of providing information that results in parts that are structurally sound and preventing the formation of defects as much as possible. Schematics showing the probable evolution of

[5] The images were recorded at a + 25° tilt with a stage rotation of 0° and 180°. This rotation results in the equivalence of a -25° tilt. The images are then appropriately mirrored to present this image.

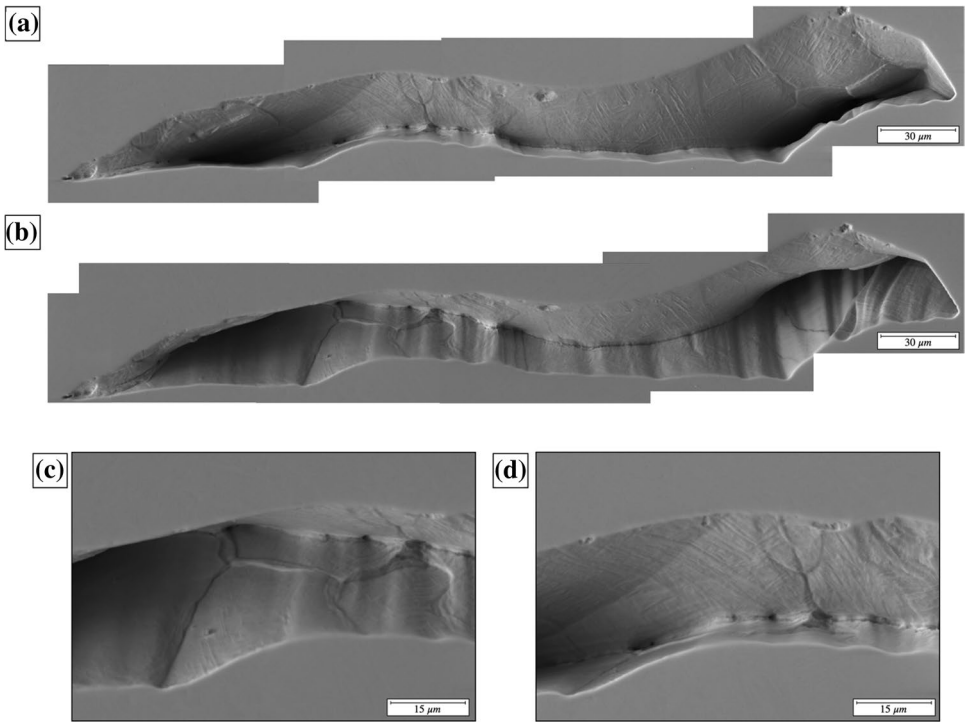

Figure 13 SEM micrographs of lack-of-fusion defect 2 of Fig. 12. (**a**, **b**) The defect tilted to image both the top and bottom at 25°. (**c**, **d**) Higher-resolution images showing grain boundaries and deformation and signatures of phase transformations

these defects have been developed and presented. The following observations can be concluded:

- Microstructural banding as a result of aluminum variations reveals information about chemical variations in the layers (solute segregation) due to fluid flow and preferential Al vaporization during melting and liquid–solid transformations in EBM Ti–6Al–4V. These bands, while not corresponding with layer thicknesses, act fairly uniformly in the planes of the molten pools. Unique compositional 'structures' reveal the relatively quick time-scale of band solidification as compared to the time-scale required for mixing. These factors together reveal

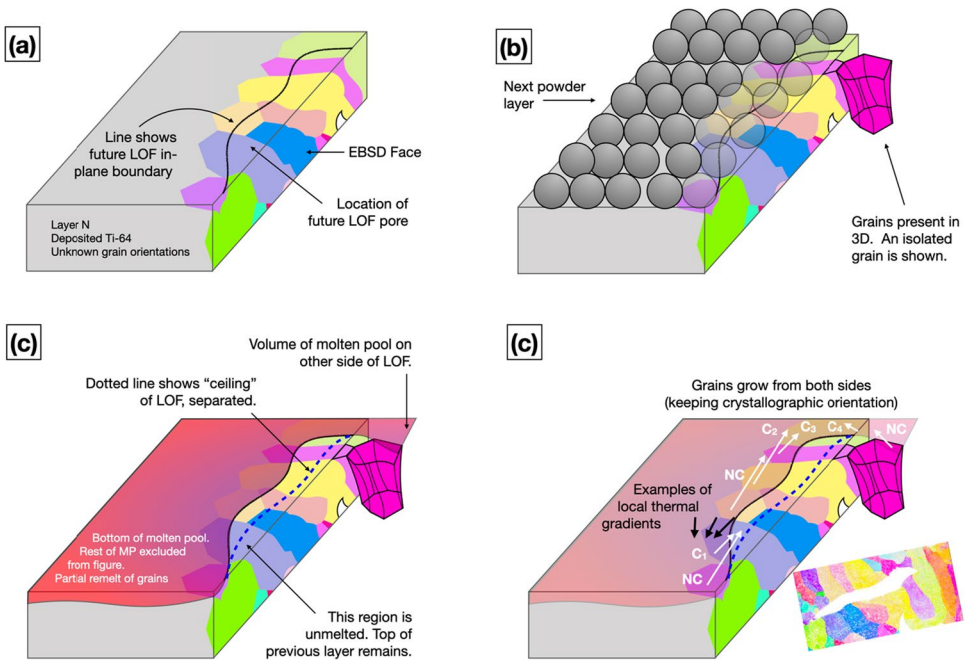

Figure 14 Schematic showing how some grains can be continuous around a LOF defect, such as LOF defect 2 of Fig. 12 (with matching grain colors). Grains that are continuous are labeled as $C_{\#}$, while the grains that are not continuous are labeled NC

that aluminum variation occurs in the liquid state within individual melt pools and varies between melt pools.
- The internal morphologies or characteristics of LOF defects, as well as the distribution of morphologies throughout the build, hint at the mechanisms of defect formation and can be used to generate models of failure modes, while the structures on the free surfaces of the defects reveal information about the local variations in fluid flow and the temperatures or times which samples were held at. Distribution information can also give insight into failure mechanisms through finite element modeling.
- Spattering can be used as a timeline variable; if observed on free surfaces, spattering must have occurred after the formation of said LOF defect surfaces, but while other aspects of the build were still partially molten or at least mushy (such as ceiling, walls, and floors). More than 40% of ejected particles landing on defect surfaces have sizes < 2.5 μm, and knowledge of the size distribution of ejecta can inform on models of the physical phenomena at play during the build process.
- Cracking can reveal information about local temperature regimes, local stresses created during liquid–solid or solid–solid transformations, the presence of other defects in their vicinity, and the role of geometry in their formation.
- Microstructural investigations near defects show the influence of heat flow interruptions during AM processes. Prior β grain growth is influenced by the morphology of LOF defects. Partially melted particles can influence the nucleation of new prior β grains.
- EBSD analysis reveals that prior β grains can grow around LOF defects, with grain growth preferred over grain nucleation.

Acknowledgements

The research was sponsored by the Department of the Navy, Office of Naval Research under ONR award number N00014-18-1-2794. Any opinions, findings, and conclusions or recommendations expressed in this material are those of the author(s) and do not necessarily reflect the views of the Office of Naval Research. Access to the Oak Ridge National Laboratory's (ORNL) additive manufacturing equipment at ORNL's Manufacturing Demonstration Facility (MDF) was facilitated by US Department of Energy's Strategic Partnership Projects (SPP) mechanism. More information can be found at https://science.energy.gov/lp/strategic-partnership-projects. Research sponsored by the U.S. Department of Energy, Office of Energy Efficiency and Renewable Energy, Industrial Technologies Program, under contract DE-AC05-00OR22725 with UT-Battelle, LLC.

Author's contribution

KO' and MJQ were involved in conceptualization, methodology, investigation, data curation, writing—original draft, writing—review and editing, and visualization. MJK was involved in methodology and investigation. PCC was involved in conceptualization, methodology, writing—review and editing, and supervision.

Data availability

As the above research is part of an ongoing project, the data are not currently available for public release.

Declarations

Conflict of interest The authors declare that they have no known competing financial interests or personal relationships that could have appeared to influence the work reported in this paper.

References

[1] Kasperovich G, Haubrich J, Gussone J, Requena G (2016) Correlation between porosity and processing parameters in TiAl6V4 produced by selective laser melting. Mater Des 105:160–170

[2] Collins PC, Brice DA, Samimi P et al (2016) Microstructural control of additively manufactured metallic materials. Annu Rev Mater Res 46:63–91. https://doi.org/10.1146/annurev-matsci-070115-031816

[3] Collins PC, Haden CV, Ghamarian I et al (2014) Progress toward an integration of process-structure-property-performance models for "three-dimensional (3-D) printing" of titanium alloys. Jom 66:1299–1309. https://doi.org/10.1007/s11837-014-1007-y

[4] Zhang Y, Bandyopadhyay A (2019) Direct fabrication of bimetallic Ti6Al4V+Al12Si structures via additive manufacturing. Addit Manuf 29:100783. https://doi.org/10.1016/j.addma.2019.100783

[5] Zhou X, Wang D, Liu X et al (2015) 3D-imaging of selective laser melting defects in a Co-Cr-Mo alloy by synchrotron radiation micro-CT. Acta Mater 98:1–16. https://doi.org/10.1016/j.actamat.2015.07.014

[6] Marini D, Corney JR (2020) Process selection methodology for near net shape manufacturing. Int J Adv Manuf Technol 106:1967–1987. https://doi.org/10.1007/s00170-019-04561-w

[7] Yan L, Chen X, Li W, et al (2020) Direct laser deposition of Ti-6Al-4V from elemental powder blends. In: Proceedings - 26th annual international solid freeform fabrication symposium - an additive manufacturing conference, SFF 2015 45:691–699

[8] King WE, Anderson AT, Ferencz RM et al (2015) Laser powder bed fusion additive manufacturing of metals; physics, computational, and materials challenges. Appl Phys Rev 2:041304. https://doi.org/10.1063/1.4937809

[9] Ahsan F, Ladani L (2020) Temperature profile, bead geometry, and elemental evaporation in laser powder bed fusion additive manufacturing process. Jom 72:429–439. https://doi.org/10.1007/s11837-019-03872-3

[10] Riveiro A, del Val J, Comesaña R, Lusquiños F, Quintero F, Boutinguiza M, Pou J (2019) Laser additive manufacturing processes for near net shape components. Near net shape manufacturing processes, p 105–141

[11] Kenney MJ, O'Donnell K, Quintana MJ, Collins PC (2021) Spherical pores as 'microstructural informants': understanding compositional, thermal, and mechanical gyrations in additively manufactured Ti-6Al-4V. Scr Mater 198:113827. https://doi.org/10.1016/j.scriptamat.2021.113827

[12] Quintana MJ, O'Donnell K, Kenney MJ, Collins PC (2021) Differences in defect distribution across scan strategies in electron beam AM Ti-6Al-4V. Adv Mater Process 179:20–23

[13] Quintana MJ, Kenney MJ, Agrawal P, Collins PC (2020) Texture analysis of additively manufactured Ti-6Al-4V deposited using different scanning strategies. Metall Mater Trans A Phys Metall Mater Sci 51:6574–6583. https://doi.org/10.1007/s11661-020-06040-4

[14] Chebil G, Bettebghor D, Renollet Y et al (2023) Deep learning object detection for optical monitoring of spatters in L-PBF. J Mater Process Technol. https://doi.org/10.1016/j.jmatprotec.2023.118063

[15] Telmen B, Szmytka F, Gloanec A-L et al (2023) Parametric analysis of direct energy deposited 316 L-Si powder on 316 L Parts. The Int J Adv Manuf Technol. https://doi.org/10.1007/s00170-023-11409-x

[16] Breuning C, Böhm J, Markl M, Körner C (2023) High-throughput numerical investigation of process parameter-melt pool relationships in electron beam powder bed fusion. Modelling 4:336–350. https://doi.org/10.3390/modelling4030019

[17] Wang P, Chen D, Tang Y et al (2023) The effect of process parameters on the stability and efficiency in the laser powder bed fusion of Ti–6Al–4V based on the interval powder layer thickness. Int J Adv Manuf Technol. https://doi.org/10.1007/s00170-023-11704-7

[18] Park S-H, Choi S, Song D-G, Jhang K-Y (2022) Microstructural characterization of additively manufactured metal components using linear and nonlinear ultrasonic techniques. Materials 15:3876. https://doi.org/10.3390/ma15113876

[19] Quintana M, Ji Y, Collins P (2022) A perspective of the needs and opportunities for coupling materials science and nondestructive evaluation for metals-based additive manufacturing. Mater Eval 80:45–63. https://doi.org/10.32548/2022.me-04256

[20] Ngo TD, Kashani A, Imbalzano G et al (2018) Additive manufacturing (3D printing): a review of materials, methods, applications and challenges. Compos B Eng 143:172–196. https://doi.org/10.1016/j.compositesb.2018.02.012

[21] Hojjatzadeh SMH, Parab ND, Yan W et al (2019) Pore elimination mechanisms during 3D printing of metals. Nat Commun 10:1–8. https://doi.org/10.1038/s41467-019-10973-9

[22] Zakaria K, Ismail Z, Redzuan N, Dalgarno KW (2015) Effect of Wire EDM cutting parameters for evaluating of additive manufacturing hybrid metal material. Procedia Manuf 2:532–537. https://doi.org/10.1016/j.promfg.2015.07.092

[23] Isakov DV, Lei Q, Castles F et al (2016) 3D printed anisotropic dielectric composite with meta-material features. Mater Des 93:423–430. https://doi.org/10.1016/j.matdes.2015.12.176

[24] Al-Bermani SS, Blackmore ML, Zhang W, Todd I (2010) The origin of microstructural diversity, texture, and mechanical properties in electron beam melted Ti-6Al-4V. Metall Mater Trans A Phys Metall Mater Sci 41:3422–3434. https://doi.org/10.1007/s11661-010-0397-x

[25] Meier C, Penny RW, Zou Y et al (2018) Thermophysical phenomena in metal additive manufacturing by selective laser melting: fundamentals, modeling, simulation, and experimentation. Ann Rev Heat Transf 20:241–316. https://doi.org/10.1615/annualrevheattransfer.2018019042

[26] Kelly SM, Kampe SL (2004) Microstructural evolution in laser-deposited multilayer Ti-6Al-4V builds: Part II. Thermal Modeling. Metall Mater Trans A Phys Metall Mater Sci 35A:1869–1879. https://doi.org/10.1007/s11661-004-0095-7

[27] Denlinger ER, Irwin J, Michaleris P (2014) Thermomechanical modeling of additive manufacturing large parts. J Manuf Sci E T ASME 136:1–8. https://doi.org/10.1115/1.4028669

[28] King W, Anderson AT, Ferencz RM et al (2015) Overview of modelling and simulation of metal powder bed fusion process at Lawrence Livermore National Laboratory. Materi Sci Technol (UK) 31:957–968. https://doi.org/10.1179/1743284714Y.0000000728

[29] Francois MM, Sun A, King WE et al (2017) Modeling of additive manufacturing processes for metals: challenges and opportunities. Curr Opin Solid State Mater Sci 21:198–206. https://doi.org/10.1016/j.cossms.2016.12.001

[30] Zhang B, Liu S, Shin YC (2019) In-Process monitoring of porosity during laser additive manufacturing process. Addit

Manuf 28:497–505. https://doi.org/10.1016/j.addma.2019.05.030
[31] Calta N (2056) Final Technical Report project title: in-situ data acquisition and tool development for additive manufacturing metal powder systems
[32] Aldrin JC, Lindgren EA (2018) The need and approach for characterization – U.S. air force perspectives on materials state awareness. AIP Conf Proc. https://doi.org/10.1063/1.5031501
[33] Buynak CF, Blackshire J, Lindgren EA, Jata KV (2008) challenges and opportunities in NDE, ISHM and material state awareness for aircraft structures: US air force perspective. In: AIP Conference Proceedings
[34] Jacobs LJ (2014) Nonlinear ultrasonics for material state awareness. In: AIP Conference Proceedings
[35] Zhang P, Liu J, To AC (2017) Role of anisotropic properties on topology optimization of additive manufactured load bearing structures. Scr Mater 135:148–152. https://doi.org/10.1016/j.scriptamat.2016.10.021
[36] Carroll BE, Palmer TA, Beese AM (2015) Anisotropic tensile behavior of Ti-6Al-4V components fabricated with directed energy deposition additive manufacturing. Acta Mater 87:309–320. https://doi.org/10.1016/j.actamat.2014.12.054
[37] Hitzler L, Hirsch J, Heine B et al (2017) On the anisotropic mechanical properties of selective laser-melted stainless steel. Materials. https://doi.org/10.3390/ma10101136
[38] Tevet O, Svetlizky D, Harel D et al (2022) Measurement of the anisotropic dynamic elastic constants of additive manufactured and wrought Ti6Al4V alloys. Materials 15(2):638. https://doi.org/10.3390/ma15020638
[39] Wolff S, Lee T, Faierson E et al (2016) Anisotropic properties of directed energy deposition (DED)-processed Ti–6Al–4V. J Manuf Process 24:397–405. https://doi.org/10.1016/j.jmapro.2016.06.020
[40] Liu Z, Zhao ZB, Liu J et al (2021) Effects of the crystallographic and spatial orientation of α lamellae on the anisotropic in-situ tensile behaviors of additive manufactured Ti–6Al–4V. J Alloys Compd. https://doi.org/10.1016/j.jallcom.2020.156886
[41] Kok Y, Tan XP, Wang P et al (2018) Anisotropy and heterogeneity of microstructure and mechanical properties in metal additive manufacturing: a critical review. Mater Des 139:565–586. https://doi.org/10.1016/j.matdes.2017.11.021
[42] Palanivel S, Dutt AK, Faierson EJ, Mishra RS (2016) Spatially dependent properties in a laser additive manufactured Ti-6Al-4V component. Mater Sci Eng, A 654:39–52. https://doi.org/10.1016/j.msea.2015.12.021
[43] Ng CH, Bermingham MJ, Dargusch MS (2023) Eliminating porosity defects, promoting equiaxed grains and improving the mechanical properties of additively manufactured Ti-22V-4Al with super-transus hot isostatic pressing. Addit Manuf 72:103630. https://doi.org/10.1016/j.addma.2023.103630
[44] Polonsky AT, Echlin MP, Lenthe WC et al (2018) Defects and 3D structural inhomogeneity in electron beam additively manufactured Inconel 718. Mater Charact 143:171–181. https://doi.org/10.1016/j.matchar.2018.02.020
[45] Zhang B, Li Y, Bai Q (2017) Defect formation mechanisms in selective laser melting: a review. Chin J Mech Eng (English Edition) 30:515–527. https://doi.org/10.1007/s10033-017-0121-5
[46] Brennan MC, Keist JS, Palmer TA (2021) Defects in metal additive manufacturing processes. J Mater Eng Perform 30:4808–4818. https://doi.org/10.1007/s11665-021-05919-6
[47] Iebba M, Astarita A, Mistretta D et al (2017) Influence of powder characteristics on formation of porosity in additive manufacturing of Ti-6Al-4V components. J Mater Eng Perform 26:4138–4147. https://doi.org/10.1007/s11665-017-2796-2
[48] Taheri H, Collins PC, Bond LJ et al (2017) Powder-based additive manufacturing - a review of types of defects, generation mechanisms, detection, property evaluation and metrology. Int J Addit Subtract Mater Manufact 1:172. https://doi.org/10.1504/ijasmm.2017.10009247
[49] Walker KF, Liu Q, Brandt M (2017) Evaluation of fatigue crack propagation behaviour in Ti-6Al-4V manufactured by selective laser melting. Int J Fatigue 104:302–308. https://doi.org/10.1016/j.ijfatigue.2017.07.014
[50] Guo Q, Chen S, Wei M et al (2020) Formation and elimination mechanism of lack of fusion and cracks in direct laser deposition 24CrNiMoY alloy steel. J Mater Eng Perform 29:6439–6454. https://doi.org/10.1007/s11665-020-05163-4
[51] Zhang T, Liu CT (2022) Design of titanium alloys by additive manufacturing: A critical review. Adv Powder Mater 1
[52] Chen Y, Clark SJ, Collins DM et al (2021) Correlative synchrotron X-ray imaging and diffraction of directed energy deposition additive manufacturing. Acta Mater. https://doi.org/10.1016/j.actamat.2021.116777
[53] Pogson S, Fox P, O'Neill W, Sutcliffe CJ (2004) The direct metal laser remelting of copper and tool steel powders. Mater Sci Eng, A 386:453–459. https://doi.org/10.1016/j.msea.2004.08.015
[54] Sames WJ, List FA, Pannala S et al (2016) The metallurgy and processing science of metal additive manufacturing. Int Mater Rev 61:315–360. https://doi.org/10.1080/09506608.2015.1116649
[55] Tiley J, Searles T, Lee E et al (2004) Quantification of microstructural features in α/β titanium alloys. Mater Sci Eng, A 372:191–198. https://doi.org/10.1016/j.msea.2003.12.008
[56] Collins PC, Welk B, Searles T et al (2009) Development of methods for the quantification of microstructural features in α + β-processed α/β titanium alloys. Mater Sci Eng, A 508:174–182. https://doi.org/10.1016/j.msea.2008.12.038
[57] Spowart JE, Mullens HM, Puchala BT (2003) Collecting and analyzing microstructures in three dimensions: a fully automated approach. JOM 55:35–37. https://doi.org/10.1007/s11837-003-0173-0
[58] Sosa JM, Huber DE, Welk B, Fraser HL (2014) Development and application of MIPAR™: a novel software package for two- and three-dimensional microstructural characterization. Integr Mater Manuf Innov 3:123–140. https://doi.org/10.1186/2193-9772-3-10
[59] Bachmann F, Hielscher R, Schaeben H (2010) Texture analysis with MTEX- Free and open source software toolbox. Solid State Phenom 160:63–68. https://doi.org/10.4028/www.scientific.net/SSP.160.63
[60] Yang Y (2015) Temperature-dependent thermoelastic analysis of multidimensional functionally graded materials. Nhk技研 151:10–17
[61] Tang M, Pistorius PC, Beuth JL (2017) Prediction of lack-of-fusion porosity for powder bed fusion. Addit Manuf 14:39–48. https://doi.org/10.1016/j.addma.2016.12.001
[62] Ivanchenko VG, Ivasishin OM, Semiatin SL (2003) Evaluation of evaporation losses during electron-beam melting of Ti-Ai-V alloys. Metall Mater Trans B 34:911–915. https://doi.org/10.1007/s11663-003-0097-7
[63] Liu J, Wen P (2022) Metal vaporization and its influence during laser powder bed fusion process. Mater Des 215:110505
[64] Tang HP, Yang GY, Jia WP et al (2015) Additive manufacturing of a high niobium-containing titanium aluminide alloy by selective electron beam melting. Mater Sci Eng, A 636:103–107. https://doi.org/10.1016/j.msea.2015.03.079

[65] Zhu Y, Tian X, Li J, Wang H (2014) Microstructure evolution and layer bands of laser melting deposition Ti-6.5Al-3.5Mo-1.5Zr-0.3Si titanium alloy. J Alloys Compd 616:468–474. https://doi.org/10.1016/j.jallcom.2014.07.161

[66] Thijs L, Verhaeghe F, Craeghs T et al (2010) A study of the microstructural evolution during selective laser melting of Ti-6Al-4V. Acta Mater 58:3303–3312. https://doi.org/10.1016/j.actamat.2010.02.004

[67] Huang N, Cook OJ, Smithson RLW et al (2022) Use of ultrasound to identify microstructure-property relationships in 316 stainless steel fabricated with binder jet additive manufacturing. Addit Manuf. https://doi.org/10.1016/j.addma.2021.102591

[68] Sotelo LD, Hadidi H, Pratt CS et al (2021) Ultrasonic mapping of hybrid additively manufactured 420 stainless steel. Ultrasonics. https://doi.org/10.1016/j.ultras.2020.106269

[69] Marshall GJ, Young WJ, Thompson SM et al (2016) Understanding the microstructure formation of Ti-6Al-4V during direct laser deposition via in-situ thermal monitoring. Jom 68:778–790. https://doi.org/10.1007/s11837-015-1767-z

[70] Akhonin SV, Trigub NP, Zamkov VN, Semiatin SL (2003) Mathematical modeling of aluminum evaporation during electron-beam cold-hearth melting of Ti-6Al-4V ingots. Metall Mater Trans B 34:447–454. https://doi.org/10.1007/s11663-003-0071-4

[71] Lee YS, Farson DF (2016) Surface tension-powered build dimension control in laser additive manufacturing process. Int J Adv Manuf Technol 85:1035–1044. https://doi.org/10.1007/s00170-015-7974-5

[72] Bayat M, Thanki A, Mohanty S et al (2019) Keyhole-induced porosities in Laser-based Powder Bed Fusion (L-PBF) of Ti6Al4V: high-fidelity modelling and experimental validation. Addit Manuf 30:100835. https://doi.org/10.1016/j.addma.2019.100835

[73] Ankem S, Scarr GK, Caplan IL, et al (1988) Multiple regression analysis of the effects of various alloying elements on the properties of titanium alloys. In: Sixth World Conference on Titanium. pp 265–268

[74] Hayes BJ, Martin BW, Welk B et al (2017) Predicting tensile properties of Ti-6Al-4V produced via directed energy deposition. Acta Mater 133:120–133. https://doi.org/10.1016/j.actamat.2017.05.025

[75] Sun Z, Tan XP, Descoins M et al (2019) Revealing hot tearing mechanism for an additively manufactured high-entropy alloy via selective laser melting. Scr Mater 168:129–133. https://doi.org/10.1016/j.scriptamat.2019.04.036

[76] Martin AA, Calta NP, Khairallah SA et al (2019) Dynamics of pore formation during laser powder bed fusion additive manufacturing. Nat Commun. https://doi.org/10.1038/s41467-019-10009-2

[77] Cunningham R, Zhao C, Parab N et al (1979) (2019) Keyhole threshold and morphology in laser melting revealed by ultrahigh-speed x-ray imaging. Science 363:849–852. https://doi.org/10.1126/science.aav4687

[78] MIPAR User Manual. https://www.manula.com/manuals/mipar/user-manual/latest/en/topic/getting-started

[79] Wolff SJ, Lin S, Faierson EJ et al (2017) A framework to link localized cooling and properties of directed energy deposition (DED)-processed Ti-6Al-4V. Acta Mater 132:106–117. https://doi.org/10.1016/j.actamat.2017.04.027

[80] Zhou S, Rabczuk T, Zhuang X (2018) Phase field modeling of quasi-static and dynamic crack propagation: COMSOL implementation and case studies. Adv Eng Softw 122:31–49. https://doi.org/10.1016/j.advengsoft.2018.03.012

[81] Borden MJ, Hughes TJR, Landis CM et al (2016) A phase-field formulation for fracture in ductile materials: finite deformation balance law derivation, plastic degradation, and stress triaxiality effects. Comput Methods Appl Mech Eng 312:130–166. https://doi.org/10.1016/j.cma.2016.09.005

[82] Borden MJ, Verhoosel CV, Scott MA et al (2012) A phase-field description of dynamic brittle fracture. Comput Methods Appl Mech Eng 217–220:77–95. https://doi.org/10.1016/j.cma.2012.01.008

[83] COMSOL Multiphysics Reference Manual. https://doc.comsol.com/5.5/doc/com.comsol.help.comsol/COMSOL_ReferenceManual.pdf

[84] Gong H, Rafi K, Gu H et al (2014) Analysis of defect generation in Ti–6Al–4V parts made using powder bed fusion additive manufacturing processes. Addit Manuf 1–4:87–98

[85] Kruth JP, Levy G, Klocke F, Childs THC (2007) Consolidation phenomena in laser and powder-bed based layered manufacturing. CIRP Ann Manuf Technol 56:730–759. https://doi.org/10.1016/j.cirp.2007.10.004

[86] Gunenthiram V, Peyre P, Schneider M et al (2018) Experimental analysis of spatter generation and melt-pool behavior during the powder bed laser beam melting process. J Mater Process Technol 251:376–386. https://doi.org/10.1016/j.jmatprotec.2017.08.012

[87] Gunenthiram V, Peyre P, Schneider M et al (2017) Analysis of laser–melt pool–powder bed interaction during the selective laser melting of a stainless steel. J Laser Appl 29:022303. https://doi.org/10.2351/1.4983259

[88] Seiler M, Patschger A, Bliedtner J (2016) Investigations of welding instabilities and weld seam formation during laser microwelding of ultrathin metal sheets. J Laser Appl 28:022417. https://doi.org/10.2351/1.4944446

[89] Fabbro R (2010) Melt pool and keyhole behaviour analysis for deep penetration laser welding. J Phys D Appl Phys. https://doi.org/10.1088/0022-3727/43/44/445501

[90] Hirth JP, Spanos G, Hall MG, Aaronson HI (1998) Mechanisms for the development of tent- shaped and invariant-plane-strain-type surface reliefs for plates formed during diffusional phase transformations. Acta Mater 46:857–868. https://doi.org/10.1016/S1359-6454(97)00302-9

[91] Seward GGE, Celotto S, Prior DJ et al (2004) In situ SEM-EBSD observations of the hcp to bcc phase transformation in commercially pure titanium. Acta Mater 52:821–832. https://doi.org/10.1016/j.actamat.2003.10.049

[92] Mullins WW (1957) Theory of thermal grooving. J Appl Phys 28:333–339

[93] Mullins WW (1958) The effect of thermal grooving on grain boundary motion. Acta Metall 6:414–427. https://doi.org/10.1016/0001-6160(58)90020-8

[94] Barrett JW, Garcke H, NÜrnberg R (2010) Finite-element approximation of coupled surface and grain boundary motion with applications to thermal grooving and sintering. Eur J Appl Math 21:519–556. https://doi.org/10.1017/S0956792510000203

[95] Khairallah SA, Anderson AT, Rubenchik A, King WE (2016) Laser powder-bed fusion additive manufacturing: physics of complex melt flow and formation mechanisms of pores, spatter, and denudation zones. Acta Mater 108:36–45. https://doi.org/10.1016/j.actamat.2016.02.014

[96] Guo Q, Zhao C, Escano LI et al (2018) Transient dynamics of powder spattering in laser powder bed fusion additive manufacturing process revealed by in-situ high-speed high-energy x-ray imaging. Acta Mater 151:169–180. https://doi.org/10.1016/j.actamat.2018.03.036

[97] Chien CY, Le TN, Lin ZH, Lo YL (2021) Numerical and experimental investigation into gas flow field and spattering phenomena in laser powder bed fusion processing of Inconel 718. Mater Des 210:110107. https://doi.org/10.1016/j.matdes.2021.110107
[98] Damkroger BK, Edwards GR, Rath BB (1989) Investigation of subsolidus weld cracking in alpha--beta titanium alloys of several alpha--beta alloys investigate, Ti--6211 was found to be susceptible to subsolidus weld cracking, pp 290–302
[99] Abbasi K, Beidokhti B, Sajjadi SA (2017) Microstructure and mechanical properties of Ti-6Al-4V welds using α, near-α and α+β filler alloys. Mater Sci Eng, A 702:272–278. https://doi.org/10.1016/j.msea.2017.07.027
[100] Lin Z, Song K, Yu X (2021) A review on wire and arc additive manufacturing of titanium alloy. J Manuf Process 70:24–45. https://doi.org/10.1016/j.jmapro.2021.08.018
[101] Banerjee D, Williams JC (2013) Perspectives on titanium science and technology. Acta Mater 61:844–879. https://doi.org/10.1016/j.actamat.2012.10.043
[102] Li GC, Li J, Tian XJ et al (2017) Microstructure and properties of a novel titanium alloy Ti-6Al-2V-1.5Mo-0.5Zr-0.3Si manufactured by laser additive manufacturing. Mater Sci Eng, A 684:233–238. https://doi.org/10.1016/j.msea.2016.11.084
[103] Lütjering G, Williams JC (2010) Titanium. Springer
[104] Kelly SM (2004) Thermal and microstructure modeling of metal deposition processes with application to Ti-6Al-4V. Mater Sci Eng 319
[105] Xu J, Zhu J, Fan J et al (2019) Microstructure and mechanical properties of Ti–6Al–4V alloy fabricated using electron beam freeform fabrication. Vacuum 167:364–373. https://doi.org/10.1016/j.vacuum.2019.06.030
[106] Stephenson PL, Haghdadi N, DeMott R et al (2020) Effect of scanning strategy on variant selection in additively manufactured Ti-6Al-4V. Addit Manuf 36:101581. https://doi.org/10.1016/j.addma.2020.101581
[107] Haghdadi N, DeMott R, Stephenson PL et al (2020) Five-parameter characterization of intervariant boundaries in additively manufactured Ti-6Al-4V. Mater Des 196:109177. https://doi.org/10.1016/j.matdes.2020.109177
[108] Shao M, Vijayan S, Nandwana P, Jinschek JR (2020) The effect of beam scan strategies on microstructural variations in Ti-6Al-4V fabricated by electron beam powder bed fusion. Mater Des 196:109165. https://doi.org/10.1016/j.matdes.2020.109165
[109] Saville AI, Vogel SC, Creuziger A et al (2021) Texture evolution as a function of scan strategy and build height in electron beam melted Ti-6Al-4V. Addit Manuf 46:102118. https://doi.org/10.1016/j.addma.2021.102118
[110] DeMott R, Haghdadi N, Liao X et al (2021) 3D characterization of microstructural evolution and variant selection in additively manufactured Ti–6Al–4V. J Mater Sci 56:14763–14782. https://doi.org/10.1007/s10853-021-06216-2
[111] Lee HJ, Aaronson HI (1988) Surface relief effects associated with Proeutectoid a plates in a Ti-7.15 wt% Cr alloy. Acta Metallurgica 36(3):787–794. https://doi.org/10.1016/0001-6160(88)90112-5